Martian phase function: Modeling the visible to near-infrared surface photometric function using HST-WFPC2 data

Jason M. Soderblom [a,*], James F. Bell III [a], Min Y.H. Hubbard [a,1], Michael J. Wolff [b]

[a] *Department of Astronomy, Cornell University, Ithaca, NY 14853-6801, USA*
[b] *Space Science Institute, 1540 30th Street, Suite 23, Boulder, CO 80303-1012, USA*

Abstract

Images of Mars in the visible to near-infrared acquired from 1996 to 2005 using the Hubble Space Telescope WFPC2 have been used to model the martian surface photometric function at 502, 673, 953, and 1042 nm. These data range in spatial resolution from 12 to 70 km/pixel at the sub-Earth point, and in phase angle coverage from 0.34° to 40.5°. The WFPC2 images have been calibrated to radiance factor or I/F and projected to a cylindrical map for coregistration and comparison to similarly mapped spacecraft data sets of albedo, topography, thermal inertia, composition, and geology. We modeled the observed I/F as a function of phase angle using Minnaert, Lambert, lunar–Lambert, and Hapke photometric functions for numerous regions of interest binned into albedo units defined by Viking and TES albedo maps, and thermal-inertia units defined by TES thermal-inertia maps. Visibly opaque water-ice clouds and data acquired under high dust opacity conditions were excluded from the analysis. Our modeling suggests that under average to low atmospheric dust opacity conditions and over this range of phase angles, the photometric properties of the martian surface at 502, 673, 953, and 1042 nm are best modeled by lunar–Lambert functions with parameters derived for three surface units defined by low, moderate, and high TES bolometric albedos.
© 2006 Elsevier Inc. All rights reserved.

Keywords: Mars, surface; Photometry; Spectrophotometry

1. Introduction

Accurate photometric characterization of a surface is required for a number of important applications in planetary science. For example, in order to accurately compare observations acquired under varying geometries and lighting conditions (e.g., data acquired from surface landers/rovers compared to data acquired from orbital platforms; Arvidson et al., 2004; Greeley et al., 2004; Poulet et al., 2004; Pinet et al., 2005) knowledge of the photometric properties of the surface are necessary. With the continued development of more complex atmospheric radiative transfer models, accurate surface photometric properties are becoming increasingly critical. For example, analysis of Mars Global Surveyor (MGS)

data for atmospheric characterization explicitly requires assumptions about the scattering properties of the surface (e.g., albedo, phase function; Smith et al., 2001; Wolff et al., 1999; Wolff and Clancy, 2003). Photoclinometry studies of Mars (e.g., Herkenhoff and Murray, 1990; Kirk et al., 2003; Soderblom and Kirk, 2003) derive digital elevation models of the martian surface near the resolution of the imaging system using photometric properties of the surface.

Estimates of the visible to near infrared martian phase function date back to as far as 1865 by Zöllner (de Vaucouleurs, 1968). More recent photometric studies of the surface materials of Mars using telescopic data (e.g., de Vaucouleurs, 1968; O'Leary and Rea, 1968; Binder and Jones, 1972; Thorpe, 1982; de Grenier and Pinet, 1995; Vdovichenko et al., 1997; Bell et al., 1999; Erard, 2000) and spacecraft data (e.g., Guinness, 1981; Arvidson et al., 1989; Johnson et al., 1999, 2006) have yielded information regarding the photometric properties of the martian surface. For example, O'Leary and Rea (1968) reported a strong opposition surge, which varied inversely with albedo

and moderate limb darkening. de Grenier and Pinet (1995) found a linear relationship between this limb darkening and albedo in the near infrared but found no such relationship in the visible. Those authors attributed at least some of this variation to increased atmospheric scattering contributions at the longer wavelengths. Bell et al. (1999) reported normal albedos and phase coefficients for various regions of interest and albedo units and found little correlation between phase coefficient and normal albedo at 1042 nm.

These properties can in turn be related to surface properties such as macroscopic surface roughness, particle size, and particle packing density. The angular width of the opposition effect has been shown to be related to surface porosity and the size distribution of the scattering particles (Helfenstein and Veverka, 1987; Hapke, 1986, 1993). The magnitude of the opposition effect has been shown to be related to particle opacity (Hapke, 1986, 1993; Domingue et al., 1997) and/or the composition and particle microstructure (Helfenstein et al., 1997). Macroscopic surface roughness is thought to represent the average surface facet tilts for all surfaces (e.g., Hapke, 1984, 1993; Helfenstein and Shepard, 1999, 2003; Cord et al., 2004). The shape of the single-particle phase function has been shown to be related to the particle shape and internal scattering (McGuire and Hapke, 1995; Hartman et al., 1996). Finally single-particle scattering albedo has been shown to be related to composition (index of refraction) and the effective particle size (Hapke, 1981, 1993; Guinness et al., 1997).

The goal of this work is to develop a simple yet accurate model of the martian surface photometric function over a wide range of phase angles applicable to telescopic, orbital, and landed surface imaging and spectroscopic observations. To this end the data presented in this paper were fit with five different photometric functions testing four different binning criteria. Section 2 discusses the data reduction and the various binning methods. The photometric functions considered are presented in Section 3. Sections 4 and 5 present and discuss the results of the various model fits.

2. Data

Data presented in this paper were acquired using the Hubble Space Telescope (HST) Wide Field/Planetary Camera 2 (WFPC2) instrument (Burrows, 1995) between 1996 and 2005 as part of a long-term observing campaign of Mars. Data were collected under HST General Observer (GO) programs 6852, 6741, 8391, 8152, 8577, 9268, and 9738, and Director's Discretionary (DD) programs 10065 and 10770 (see Table 1). While these data were acquired through many WFPC2 filters, this study utilizes data acquired through four of these filters common to most of the measurements and spanning a wide range of wavelengths: F502N, F673N, F953N, and F1042M. Data acquired at shorter wavelengths through the F410M filter are also used to characterize the atmosphere at the time of the observations. The effective center wavelength and bandwidth for each of these filters are listed in Table 2.

The data were processed and calibrated to units of flux or radiance (W cm^{-2} nm^{-1} sr^{-1}) following the procedures de-

scribed by Lauer (1989) and Holtzman et al. (1995a, 1995b), using calibration files described by Holtzman et al. (1995a, 1995b) and Baggett et al. (1996). Further calibration of the data to radiance factor or I/F (where I is the radiance observed from the scene and πF is the incident solar irradiance at the top of the martian atmosphere at the time of the observation convolved to the bandpass of the relevant filter) is described in Bell et al. (1999) and Wolff et al. (1999). The absolute photometric errors in I/F for these data are conservatively estimated to be between 5 and 10% of the radiance values (Bell et al., 1997).

The data were projected to equal-area Mollweide projection maps using the procedure outlined in Bell et al. (1997), resampled to 1° pixel^{-1} in order to increase the signal to noise, and coregistered to similarly mapped spacecraft data sets of albedo, topography, thermal inertia, composition, and geology. In order to reduce residual coregistration errors and decrease the computational time for the photometric modeling, the WFPC2 data were also resampled to a set 10° pixel^{-1} maps prior to modeling. Further details of the calibration of these data can be found in Bell et al. (1997, 1999) and Wolff et al. (1997, 1999).

For comparison with previous and historical telescopic photometric observations of Mars, the whole-disk averaged I/F versus phase angle for the four wavelengths being considered (502, 673, 953, and 1042 nm) have been plotted in Fig. 1. The data shown in these plots have not been corrected for the different orientations (central meridian longitudes, subsolar latitudes) of Mars within the data set, and therefore some of the observed variations may be due to the different percentages of high-albedo versus low-albedo topography observed in each image. Additionally, no considerations have been made for the atmospheric contributions to the observed reflectance.

For the purposes of generating a small set of simple accurate martian photometric functions, the data were binned according to various surface properties into smaller subsets to be modeled. Data were binned according to bolometric albedo defined by the data from the Viking Orbiter Infrared Thermal Mapper (IRTM) for 0.3–3.0 μm (Pleskot and Miner, 1981; Paige et al., 1994; Paige and Keegan, 1994), bolometric albedo defined by the Mars Global Surveyor Thermal Emission Spectrometer (TES) for 0.3–2.9 μm (Christensen et al., 2001), and by thermal inertia derived from TES (Mellon et al., 2000). Bin numbers and sizes were varied in an effort to identify the best photometric subregions. For each binning criteria mentioned above, four sets of bins were considered: two, three, four, and five bins. In each case bins were equal in size and regularly spaced. For example, in the case of three TES albedo bins, three bins of size 0.067 ranging from 0.110 to 0.177, 0.177 to 0.243, and 0.243 to 0.310 were used to sort data for modeling. Figs. 2, 3, and 4 show maps of these bins.

Data were also binned into several geographic regions selected to represent a range of surface types. Mare Acidalium, for example, was selected for its low albedo and moderate thermal inertia. Syrtis Major was included as an example of low albedo, low thermal inertia material. Arabia Terra was selected to represent high albedo and low thermal inertia terrains. Amazonis Planitia was chosen as a low thermal inertia exam-

Table 1
HST WFPC2 observations of Mars used in this study: 1996–2005

UT date yymmdd	Time (UT)	Wavelengths (nm)	Diam. (″)	SE lat. (°)	SE lon. (°)	Phase[a] (°)	L_s (°)	Res.[b] (km pix^{-1})	PROGID[c]	Dust[d] opacity
				HST Cycle 6 WFPC2 Data						
960918	20:14	410, 502, 673, 953, 1042	4.6	16.77	162.34	29.32	11.29	67.4	6741, James	0.32
961015	14:03	410, 502, 673, 953, 1042	5.1	21.26	170.09	32.68	23.95	61.5	6741, James	0.25
961129	18:08	410, 502, 673, 953, 1042	6.4	24.46	154.60	36.34	44.50	48.9	6741, James	0.24
970104	0:16	410, 502, 673, 953, 1042	8.3	23.78	270.46	35.11	60.07	37.7	6741, James	0.24
970104	17:50	410, 502, 673, 953, 1042	8.3	23.75	167.06	35.02	60.39	37.5	6741, James	0.24
970330	4:13	410, 502, 673, 1042	14.0	23.38	284.01	10.73	97.44	22.3	6741, James	0.21
970330	10:40	410, 502, 673, 1042	14.0	23.38	18.41	10.93	97.56	22.3	6741, James	0.21
970330	15:35	410, 502, 673, 1042	14.0	23.39	90.37	11.09	97.65	22.3	6741, James	0.21
970330	22:15	410, 502, 673, 1042	14.0	23.40	187.94	11.30	97.78	22.4	6741, James	0.21
970417	22:19	410, 502, 673, 953	12.7	24.02	29.56	23.57	105.86	24.6	6741, James	0.22
970517	17:27	410, 502, 673, 953, 1042	10.1	25.30	43.02	35.58	119.56	31.0	6741, James	0.17
970518	2:44	410, 502, 673, 953, 1042	10.1	25.32	178.65	35.68	119.74	31.1	6741, James	0.17
970518	9:11	410, 502, 673, 953, 1042	10	25.33	272.88	35.74	119.87	31.1	6741, James	0.17
970604	1:18	410, 502, 673, 953, 1042	8.9	25.91	357.20	38.80	127.75	35.2	6793, Smith	0.18
970627	14:02	410, 502, 673, 953, 1042	7.6	25.99	322.66	40.48	139.19	41.0	6741, James	0.18
970627	17:15	410, 502, 673, 953, 1042	7.6	25.98	9.61	40.48	139.25	41.1	6741, James	0.18
970627	20:29	410, 502, 673, 953, 1042	7.6	25.98	56.81	40.49	139.32	41.1	6741, James	0.18
				HST Cycle 8 WFPC2 Data						
990427	18:05	410, 502, 673, 953, 1042	16.2	18.96	19.09	2.70	130.50	19.4	8152, Bell	0.18
990428	0:32	410, 502, 673, 953, 1042	16.2	19.00	113.49	2.92	130.63	19.3	8152, Bell	0.18
990501	13:57	410, 502, 673, 953, 1042	16.2	19.54	283.61	5.90	132.35	19.3	8152, Bell	0.18
990506	11:37	410, 502, 673, 953, 1042	16.1	20.26	205.66	10.00	134.74	19.4	8152, Bell	0.18
				HST Cycle 9 WFPC2 Data						
010116	16:08	410, 502, 673, 953, 1042	5.7	15.29	359.58	34.95	103.96	54.6	8577, James	0.22
010213	10:56	410, 502, 673, 953, 1042	6.9	9.45	14.62	37.54	116.66	45.3	8577, James	0.21
010402	15:55	410, 502, 673, 953, 1042	10.6	0.50	351.06	36.46	139.75	29.6	8577, James	0.19
010513	17:23	410, 502, 673, 953, 1042	16.4	−1.51	352.05	23.18	160.80	19.1	8577, James	0.23
				HST Cycle 10 WFPC2 Data						
010626	19:35	410, 502, 673, 953, 1042	20.7	5.38	351.85	11.81	185.12	15.1	9268, Noll	0.33[e]
010626	19:53	410, 502, 673	20.7	5.39	356.24	11.82	185.12	15.1	9268, Noll	0.33[e]
				HST Cycle 12 WFPC2 Data						
030821	11:23	410, 502, 673	25.0	−18.96	197.94	8.13	245.3	12.5	9738, Bell	0.63
030822	4:51	410, 502, 673	25.0	−18.94	93.50	7.63	245.77	12.5	9738, Bell	0.63
030826	22:43	410, 502, 673	25.1	−18.81	319.59	5.12	248.78	12.4	10065	0.63
030827	9:56	410, 502, 673	25.1	−18.81	123.71	5.00	249.07	12.4	10065	0.63
				HST Cycle 14 WFPC2 Data						
051107	4:42	410, 502, 673, 953, 1042	19.9	−15.61	219.81	0.34	319.81	15.7	10770	1.0[f]

[a] Each pixel in our disk-resolved images of Mars has a different incidence and emission angle that can be derived from ephemeris information at the time of each observation. However, the *difference* between the incidence and emission angles—the phase angle—is a constant for every pixel on the disk, at the scale of these telescopic observations.

[b] Resolution is the best spatial resolution at the sub-Earth point for images obtained on the PC1 chip.

[c] Space Telescope Science Institute Program Identification number and Principal Investigator, for HST data archive access.

[d] TES thermal-infrared dust opacities (Smith et al., 2000) were averaged over 10° of L_s around the observation dates in 1996 and 1997, and over a two-week period around observation dates 1999 and onward. Averages were taken from 0° to 30° N latitude and over all longitudes. These opacities were increased by 30% to convert from $\tau_{absorbed}$ to $\tau_{extinction}$ (Wolff and Clancy, 2003) and then by a factor of 1.7, the estimated ratio of optical to infrared opacity in the martian atmosphere (Clancy et al., 2003).

[e] TES thermal-infrared dust opacity for 010626 was estimated by averaging opacities only for the week prior to the observation date, to avoid including higher opacities in the average from a dust storm that occurred just after this date.

[f] Optical dust opacity for 051108 was estimated by averaging the visible optical depths measured by the Mars Exploration Rovers Spirit and Opportunity landing sites using Pancam 440 and 880 nm direct solar imaging from the surface (Lemmon et al., in preparation).

Table 2
HST WFPC2 filters

Filter name	Effective center wavelengths (nm)	Bandwidth (nm)
F410M	408.8	14.7
F502N	501.2	2.7
F673N	673.2	4.7
F953N	954.5	5.3
F1042M	1022.8	44.9

ple. Other regions considered included Hellas Planitia, Utopia Isidis, and Tharsis but were not included as these regions could not be adequately modeled given the available data. Because these geographic regions were on the order of the pixel size at $10°$ pixel^{-1}, a set of $5°$ pixel^{-1} maps were employed for the geographic bins despite the small increased error introduced by residual coregistration errors of the WFPC2 data. The geographic regions selected are shown in Fig. 5 on a TES albedo map resampled to $5°$ pixel^{-1}.
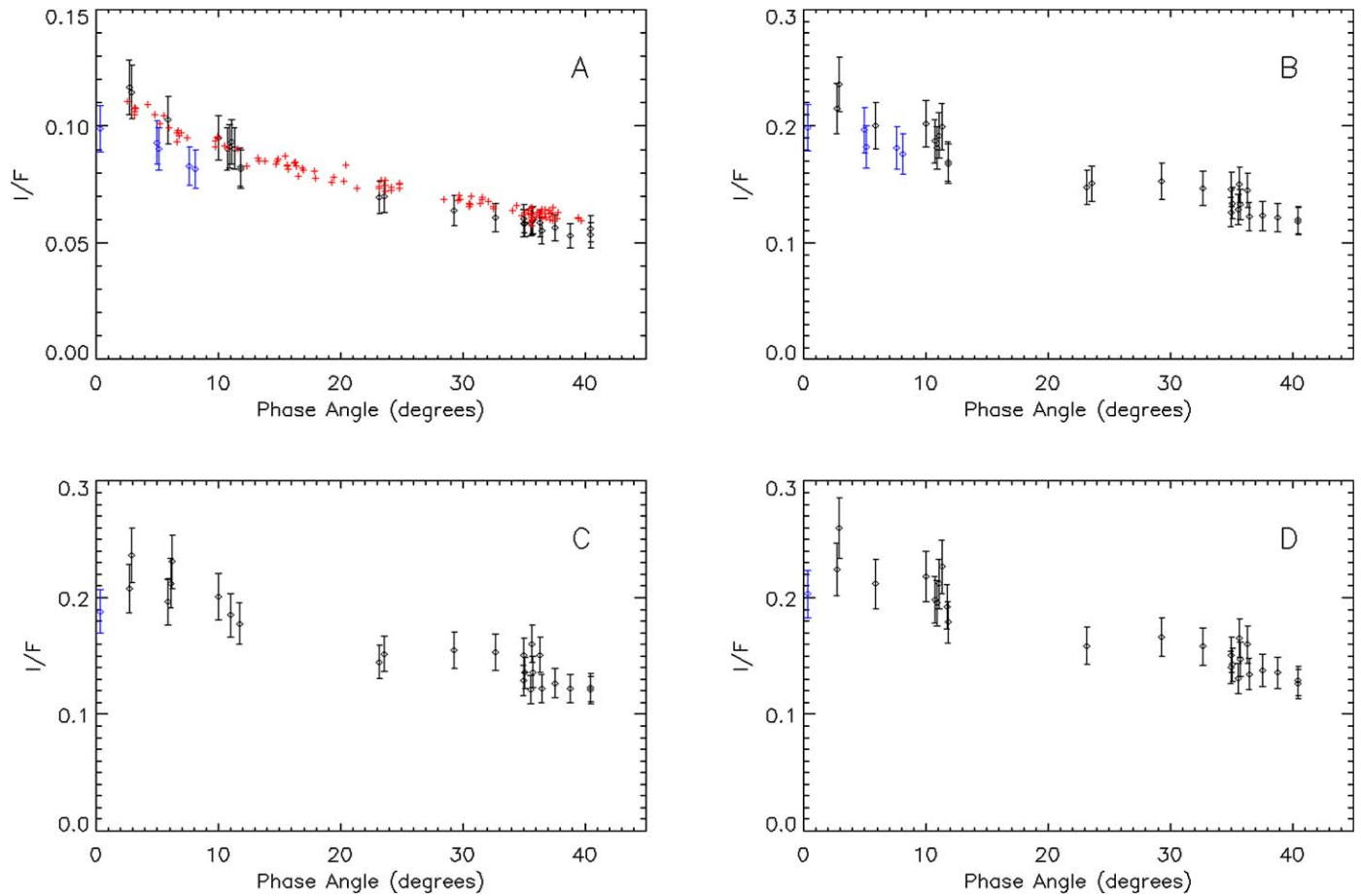
Fig. 1. Plots of whole-disk averaged martian reflectance versus phase angle for (A) 502, (B) 673, (C) 952, and (D) 1042 nm. WFPC2 data are plotted as open diamonds, with data acquired under periods of high opacity ($\tau > 0.5$) plotted in blue. WFPC2 data have not been corrected for rotation. For comparison V-band observations acquired between 1954 and 1965 (Young, 1975, and references within) scaled to the HST data at $\sim$10° phase are plotted as red pluses with the 502 nm observations.
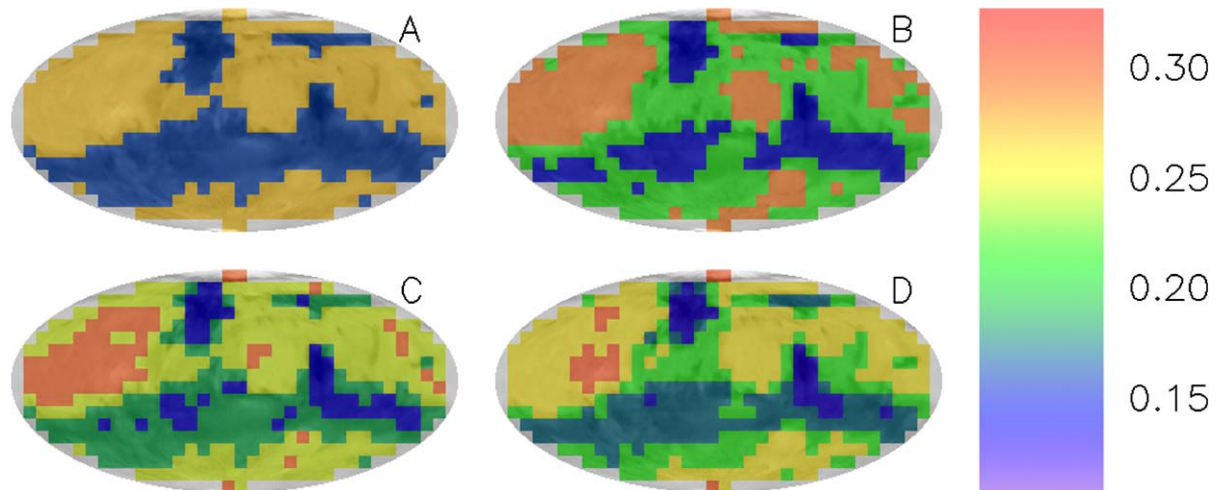

Fig. 2. Maps of two (A), three (B), four (C), and five (D) bins derived from Viking IRTM bolometric albedo data from Pleskot and Miner (1981), Paige et al. (1994), and Paige and Keegan (1994) overlain on a Viking IRTM bolometric albedo map. Colors correspond to albedo at the bin center. Data were binned according to various surface properties including IRTM bolometric albedo. Model fits of the data binned via these different techniques were compared.

Visibly opaque water-ice clouds were excluded from the analysis by identifying all pixels with a reflectance at 410 nm above a threshold value that is a function of phase angle. The 410 nm images were first normalized to zero incidence

and emission by performing a simple Minnaert correction (Minnaert, 1941) using an average value of $k = 0.7$, consistent with previous photometric studies (e.g., Binder and Jones, 1972; Erard et al., 1994; de Grenier and Pinet, 1995;
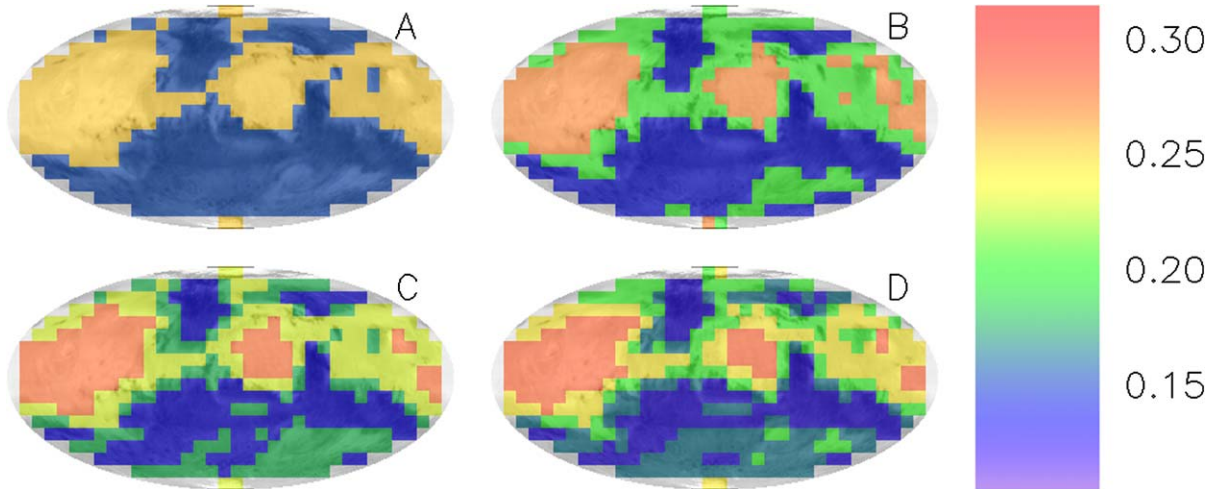
Fig. 3. Maps of two (A), three (B), four (C), and five (D) bins derived from TES bolometric albedo data from Christensen et al. (2001) overlain on a TES bolometric albedo map. Colors correspond to albedo at the bin center. Data were binned according to various surface properties including TES bolometric albedo. Model fits of the data binned via these different techniques were compared.
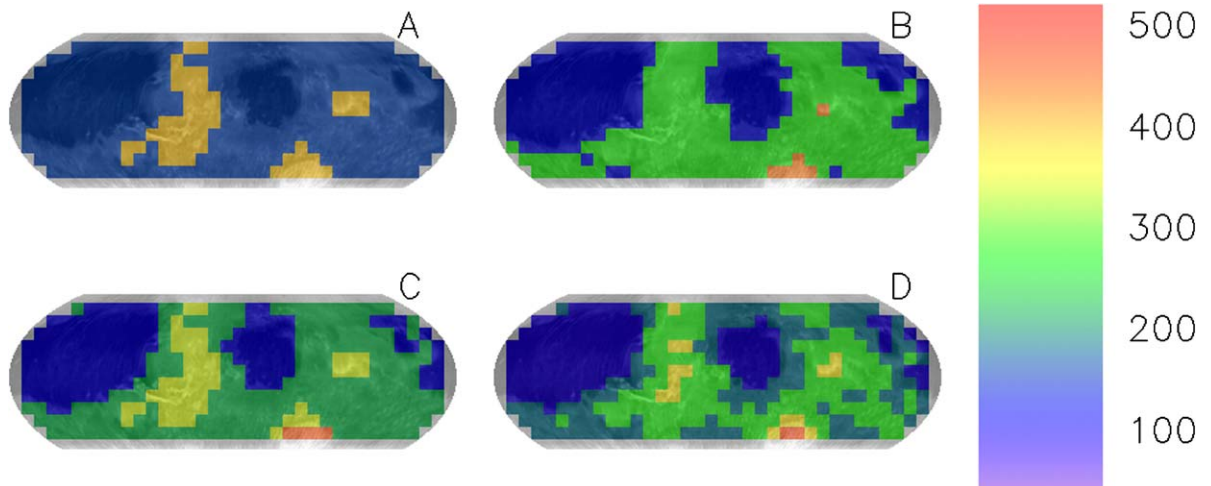

Fig. 4. Maps of two (A), three (B), four (C), and five (D) bins derived from TES thermal inertia data from Mellon et al. (2000) overlain on a TES thermal inertia map. Colors correspond to thermal inertia at the bin center in units of $J\,m^{-2}\,K^{-1}\,s^{-1/2}$. Thermal inertia data are not available at high latitudes thus these maps are truncated at $\pm 57°$ latitude. Data were binned according to various surface properties including TES thermal inertia. Model fits of the data binned via these different techniques were compared.
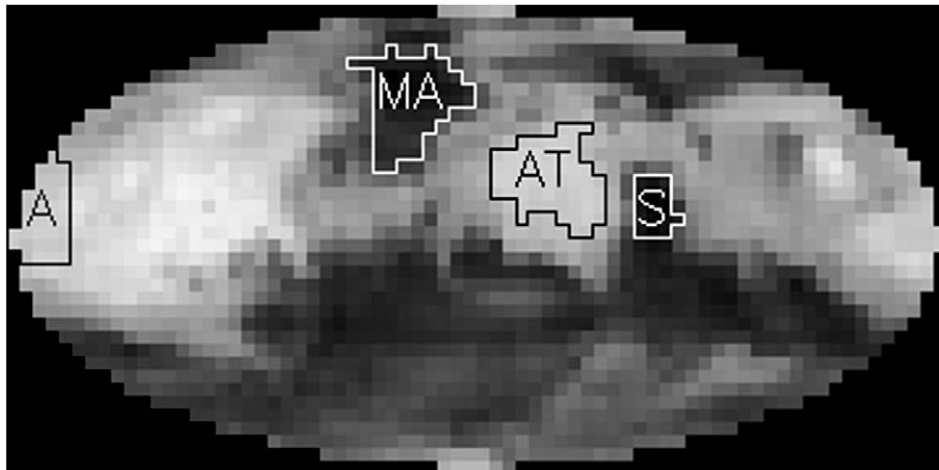

Fig. 5. Map of geologic units used to bin the data are shown on a TES bolometric albedo map resampled to $5°\,pixel^{-1}$. Geographic regions shown are: Mare Acidalium (MA), Amazonis Planitia (A), Arabia Terra (AT), and Syrtis Major (S).
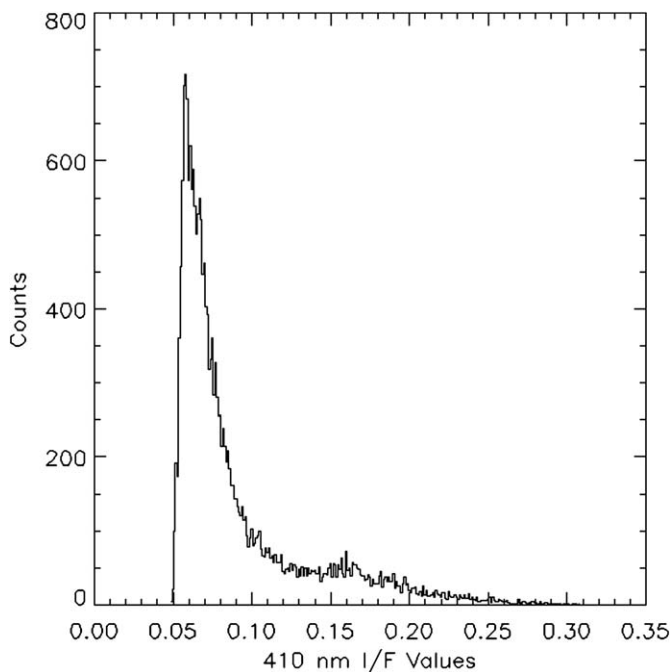
Fig. 6. Example histogram of the 410 nm Minnaert-corrected data used to derive the surface/cloud threshold values used to exclude water-ice clouds from the data. The threshold was defined as the median value of the surface pixels plus the half-width at half-max of the distribution of surface pixels. In this example for 10° phase, a median value of the surface pixels was determined to be 0.58 with a full-width at half-max of 0.03, giving a threshold of 0.073 at 10° phase.
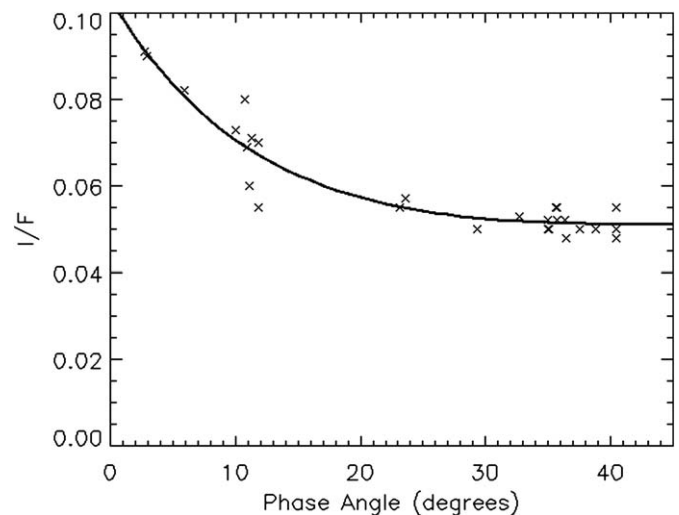

Fig. 7. Surface/cloud $I/F_{410\,nm}$ thresholds measured from histogram plots of the 410 nm Minnaert-corrected data (e.g., Fig. 6) plotted as a function of phase angle. The solid line is an exponential curve, $0.043 + 0.0084\alpha + 0.060 \times e^{(-4.8\alpha)}$, fit to the data. The threshold values calculated from this expression were used to identify and thereby remove water-ice clouds from the HST data.

Bell III et al., 1999; Esposito et al., 2006). Next, to define the threshold value, reflectance histograms of the Minnaert-corrected 410 nm data were plotted for each phase angle. These histograms show a bimodal distribution of pixels containing sunlight reflected from the surface and from clouds. An example of these histograms is plotted in Fig. 6. From these plots a threshold was defined for each image as the median value of the surface pixels plus the half-width at half-max of the distribution of surface pixels. To reduce the error introduced by any single measurement the calculated threshold values for each phase angle were fit with an exponential curve (see Fig. 7),

$$\text{threshold}_{410\,nm}(\alpha) = 0.043 + 0.0084\alpha + 0.060 \times e^{(-4.8\alpha)},$$

given in terms of the phase angle (α) in radians. Values from this expression were used to identify and thereby exclude regions of high atmospheric opacity in the 410 nm data. These regions were then excluded from data in all wavelengths concurrently acquired with the 410 nm observations, thus resulting in a first order removal of atmospheric "contamination" due to clouds in our surface-oriented phase function study.

The effects of scattering from dust in the martian atmosphere on modeling the surface photometric properties have been discussed in detail by several authors using telescopic or orbiter data (e.g., Mead, 1970; Thorpe, 1982; Erard et al., 1994) and measurements obtained from the surface (e.g., Tomasko et al., 1999; Thomas, 2001; Johnson et al., 2006). Unlike the color of the Earth's sky on a cloud-free day (which is controlled by

molecular Rayleigh scattering), the color of the martian sky is dominated by the scattering properties of dust aerosol particles with sizes comparable to (or larger than) visible light. As a result, the strongly absorbing nature of the dust at blue wavelengths (e.g., Pollack et al., 1979; Tomasko et al., 1999, and references within) produces diffuse illumination that is significantly reddened from that of the incident sunlight. For example, at the Mars Pathfinder landing site and under moderate levels of dust opacity (τ), estimates suggest that as much as 40% of the illumination of the surface is from diffusely-scattered sky light (Thomas, 2001). As another example, Johnson et al. (2006) estimated that on sol 13 of the Mars Exploration Rover *Spirit* mission, the diffuse component of the surface reflectance at 750 nm accounted for 7–36% of the observed reflectance ($\tau \approx 0.9$; Lemmon et al., in preparation).

Scattering of incident solar irradiation by aerosols in the martian atmosphere also decreases the absolute brightness of Mars as observed from above the atmosphere in telescopic or orbital measurements. Fig. 1 demonstrates the effect of increased τ as retrieved from TES (Smith et al., 2000) on the observed above-atmosphere reflectance of Mars. Whole-disk average reflectances acquired with $\tau \sim 0.6$ are seen to be 10–20% lower than whole-disk average reflectances acquired under similar viewing geometries but with lower atmospheric dust opacities.

In this HST-based photometric study we have not attempted to model the scattering from atmospheric dust; however, we have attempted to minimize the errors introduced by aerosol scattering in our models by selecting data that have low dust opacities. To this end we have excluded all data acquired under optical dust opacities of 0.5 and greater. These data have been highlighted in Fig. 1. While there are limitations to such an approach, we believe that it is a necessary first step in determining the surface scattering properties.
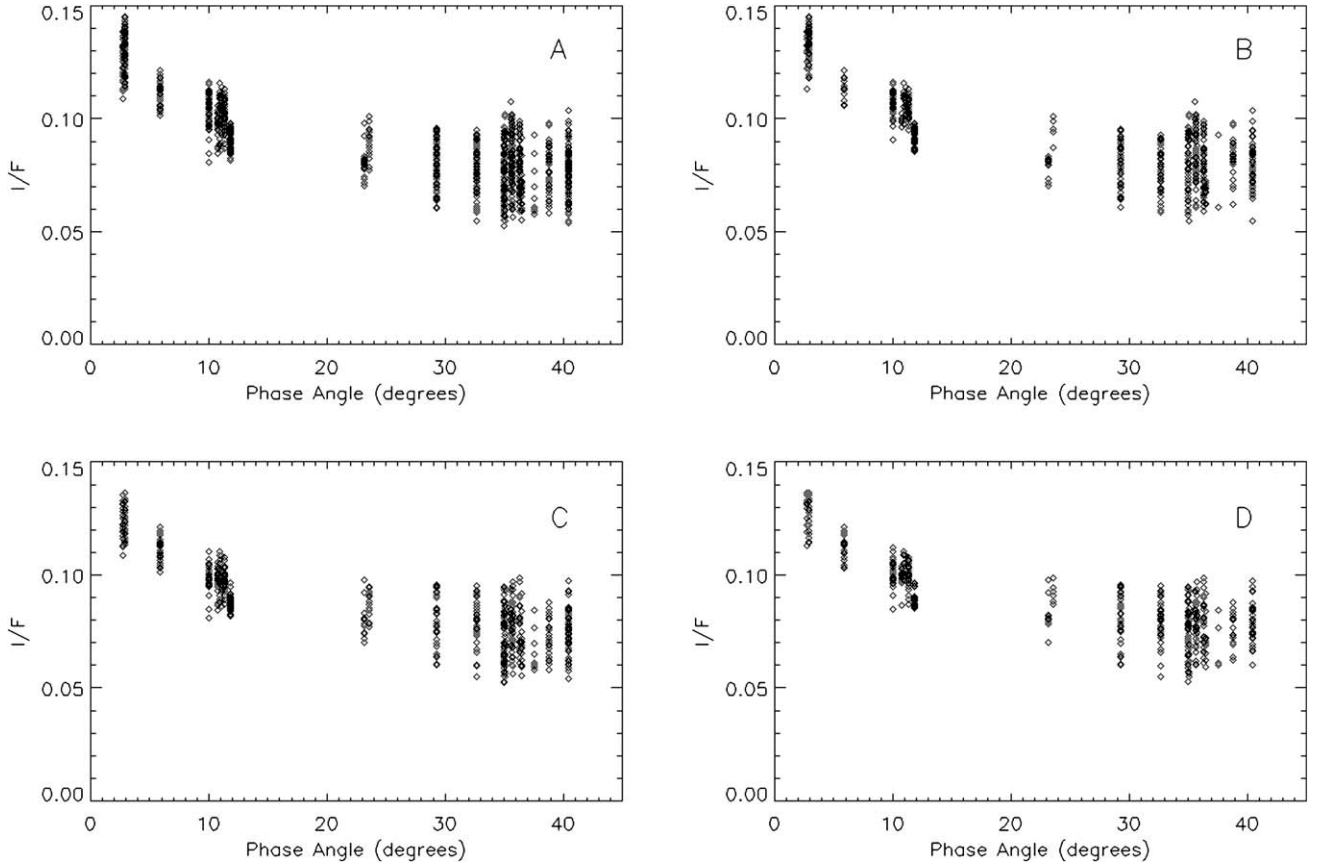
Fig. 8. I/F versus phase for 502 nm data binned by TES bolometric albedo. For each frame plotted data represent data from a single bin. (A) Data sorted into two bins; data plotted are from an albedo bin ranging from 0.21 to 0.31. (B) Data sorted into three bins; data plotted are from an albedo bin ranging from 0.24 to 0.31. (C) Data sorted into four bins; data plotted are from an albedo bin ranging from 0.21 to 0.26. (D) Data sorted into five bins; data plotted are from an albedo bin ranging from 0.23 to 0.27. Data shown in these plots have incidence and emission angles less than 60°.

Figs. 8 and 9 are representative phase plots of these data binned by various surface properties. Fig. 8 provides an example of the effect of varying bin sizes in our study (shown are phase plots for 502 nm data sorted by TES bolometric albedo into two to five albedo bins). Fig. 9 compares data binned according to the various surface properties discussed above; frames A through D show I/F versus phase for the 502 nm data binned by Viking bolometric albedo, TES bolometric albedo, and TES thermal inertia, and data from a representative geographic region: Mare Acidalium.

3. Photometric models

The goal of this work is to develop a simple yet accurate model of the martian surface photometric function over a wide range of phase angles applicable to telescopic, orbital, and landed surface imaging and spectroscopic observations. Thus, we considered four general classes of photometric functions when modeling our observations: Lambert, Minnaert, lunar–Lambert, and Hapke. These models describe the variations in I/F as a function of the viewing geometry expressed as the cosine of the incidence and emission angles, μ_0 and μ, respectively, and α.

3.1. Lambert function

The Lambert function (Lambert, 1760) is represented by a simple decrease in I/F with μ_0, and does not exhibit any specific dependence on α:

$$I(\mu_0)/F = A_L \mu_0. \tag{1}$$

The Lambert albedo, A_L, is the fraction of incident solar irradiance scattered off the surface into solid angle π (Hapke, 1993).

3.2. Minnaert function

The Minnaert function (Minnaert, 1941) expands upon the Lambert function by introducing an additional term dependent on the cosine of the emission angle as well as the Minnaert index, k, an empirical constant that sets the weighting between the incidence and emission angle contributions:

$$I(\mu, \mu_0)/F = \pi A_M \mu_0^k \mu^{k-1}, \tag{2}$$

where the Minnaert albedo, A_M, is the fraction of incident solar irradiance scattered normally from a normally illuminated surface. While k and A_M can depend on phase (Hapke, 1993) previous implementation of this function for use with martian data have often treated it as a constant for all phase angles (e.g., de Grenier and Pinet, 1995; Bell et al., 1997, 1999).
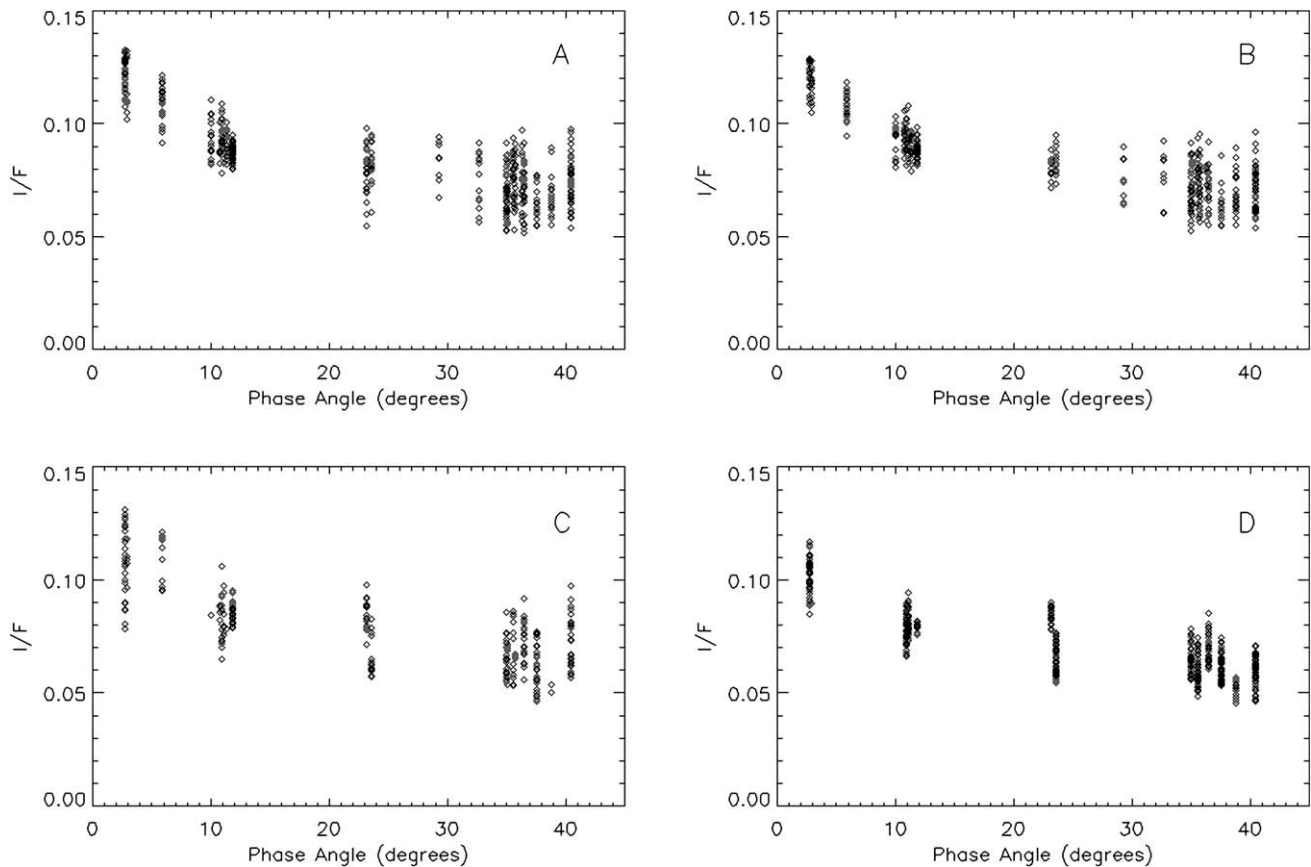
Fig. 9. I/F versus phase for 502 nm data binned according to various surface properties. (A) Data have been binned into five Viking bolometric albedo bins; data plotted have an albedo of 0.20 to 0.24. (B) Data have been binned into five TES bolometric albedo bins; data plotted have an albedo of 0.19 to 0.23. (C) Data have been binned into five TES thermal inertia bins; data plotted have a thermal inertia of 290 to 410 $\mathrm{J\,m^{-2}\,K^{-1}\,s^{-1/2}}$. (D) Data plotted are from Mare Acidalium. All data plotted have incidence and emission angles less than 60°.

3.3. Lunar–Lambert function

Chandrasekhar (1960) derived a photometric function now known as the Lommel–Seeliger lunar function from the laws of radiative transfer to describe the scattering properties of the dark surface of the Moon:

$$I(\mu, \mu_0, \alpha)/F = (w/4)\big(\mu_0/(\mu + \mu_0)\big) f(\alpha), \qquad (3)$$

where w is the single-scattering albedo and $f(\alpha)$ is an arbitrary function describing the phase dependence of the surface scattering function.

Meador and Weaver (1975) present a simple function that adequately models the photometric properties of most surfaces as a linear combination of a Lambert function (Eq. (1)) and the Lommel–Seeliger lunar function (Eq. (3)). Combining Eqs. (1) and (3), the lunar–Lambert function may be expressed as

$$I(\mu, \mu_0, \alpha)/F = A f(\alpha)\big(\mu_0/(\mu + \mu_0)\big) + B\mu_0, \qquad (4)$$

where A and B are empirical parameters that determine the relative lunar-like and Lambert contributions to the scattering function, respectively.

Comparative studies of photometric functions (Gradie and Veverka, 1984; McEwen, 1991) have shown that for most surfaces observed in the Solar System both the so-called "lunar–Lambert" and the Minnaert functions can provide adequate

photometric fits for surfaces that are accurately described by Hapke's photometric function; however, the lunar–Lambert function provides a superior fit compared to a Minnaert function for surfaces with a macroscopic surface roughness (measured as the mean slope of the surface) of less than 30° (McEwen, 1991), macroscopic surface roughness for most martian surfaces has been estimated to be between 2° and 25° (Arvidson et al., 1989; Guinness et al., 1997; Johnson et al., 1999, 2006). The lunar–Lambert function has been used to study the photometric properties of various planetary surfaces and laboratory samples (e.g., Meador and Weaver, 1975; Squyres, 1981; Squyres and Veverka, 1981; Buratti, 1983; Buratti and Veverka, 1983; Buratti, 1984; Gradie and Veverka, 1984; Buratti, 1995; McEwen, 1986; Sullivan et al., 1996; Pappalardo et al., 1998; Geissler et al., 1998, 1999).

3.3.1. Empirical lunar–Lambert function

Squyres (1981) used an empirical expression for $f(\alpha)$ in modeling the scattering properties of the surfaces of Ganymede, Callisto, Phobos, and the Moon. He combined a linear term to describe the scattering at larger phase and an exponential term to describe the scattering at low phase. This expression can be written as

$$f(\alpha) = C + D\alpha + E e^{-F\alpha}, \qquad (5)$$

where C, D, E, and F are arbitrary constants. Using Eq. (5) to express $f(\alpha)$, the lunar–Lambert function can be written as

$$I(\mu, \mu_0, \alpha)/F = A\big(C + D\alpha + Ee^{-F\alpha}\big)$$
$$\times \big(\mu_0/(\mu + \mu_0)\big) + B\mu_0. \qquad (6)$$

A further simplification used by Meador and Weaver (1975) and Buratti (1983) to reduce the number of free parameters is to set $B = 1 - A$. The resulting equation,

$$I(\mu, \mu_0, \alpha)/F = A\big(C + D\alpha + Ee^{-F\alpha}\big)$$
$$\times \big(\mu_0/(\mu + \mu_0)\big) + (1 - A)\mu_0 \qquad (7)$$

will be referred to as the "empirical lunar–Lambert function" in this study.

3.3.2. HG lunar–Lambert function

Buratti et al. (2004) presented an expression for $f(\alpha)$ in terms of a single-particle phase function $p(\alpha)$, a function describing the opposition effect $B(\alpha)$, and $S(\mu, \mu_0, \alpha)$, a term that describes the macroscopic surface roughness, as:

$$f(\alpha) = p(\alpha)B(\alpha)S(\mu, \mu_0, \alpha). \qquad (8)$$

Henyey and Greenstein (1941) derived a single-particle phase function $p(\alpha)$ as an empirical equation in terms of an asymmetry factor, ζ (constrained to be between -1 and 1), that describes the scattering properties of the individual particles as

$$p(\alpha) = \big(1 - \zeta^2\big)/\big(1 + 2\zeta\cos(\alpha) + \zeta^2\big)^{3/2}. \qquad (9)$$

The Henyey–Greenstein function (hereafter referred to as the HG function) is isotropic when $\zeta = 0$, forward scattering when $\zeta = 1$, and backscattering when $\zeta = -1$ (Hapke, 1993). Because this expression has only one parameter to describe the scattering distribution, many authors choose to use a two-term HG function, a linear combination of two HG functions of opposite sign to independently describe the forward and backward lobes (e.g., Domingue et al., 1991, 1997; Domingue and Hapke, 1992; Hapke, 1993; Hapke et al., 1998). In this study, however, the one-term HG function is preferred over the two-term HG function due to the fact that the forward scattering lobe cannot be adequately constrained by the primarily backscattering viewing geometries available in our HST data set.

The second term in Eq. (8) ($B(\alpha)$) describes the opposition effect, a non-linear increase in brightness near zero phase. Two processes must be considered when examining the opposition effect: the shadow-hiding opposition effect (SHOE), and the coherent backscatter opposition effect (CBOE) (Shkuratov and Muinonen, 1992; Helfenstein et al., 1997; Hapke et al., 1998; Hapke, 2002). The CBOE is confined to very small phase angles, and the SHOE dominates at phase angle above $\sim3°$ (Helfenstein et al., 1997; Hapke et al., 1993, 1998). Due to limited low τ coverage below $5°$ phase, the CBOE is neglected in our study.

An expression for the SHOE is derived in Hapke (1986, 1993) in terms of the amplitude B_{so} and the angular extent h_s of the SHOE as

$$B_{sh}(\alpha) = 1 + B_{so}\big(1 + (1/h_s)\tan(\alpha/2)\big)^{-1}. \qquad (10)$$

The amplitude of the SHOE is related to the opacity of the scattering particles; in the limiting case of $B_{so} = 1$, the particles are opaque and all the light is scattered off the surface (Hapke, 1986, 1993). The angular width of the SHOE, h_s, is related to the particle size distribution and surface packing density, with larger values of h_s corresponding to more closely packed surfaces and/or more uniform grain size distributions (Hapke, 1986, 1993).

The third term in the expression for $f(\alpha)$ in Eq. (8) describes the macroscopic surface roughness. However, Helfenstein and Veverka (1989) have shown that data at large phase angles ($>50°$) are needed in order to constrain the macroscopic roughness. As our data only extend to $\sim40°$, macroscopic roughness is neglected as a variable parameter. Reported values for martian macroscopic surface roughness vary with surface type by an order of magnitude; Arvidson et al. (1989), Guinness et al. (1997), and Johnson et al. (1999, 2006) report values for between $2°$ and $25°$ for a range of surface types. With no reasonable average value for macroscopic roughness, the term expressing macroscopic roughness is not included in this study. This is equivalent to setting the macroscopic surface roughness to zero.

Using Eqs. (9) and (10) for the single-particle phase function $p(\alpha)$ and the opposition effect amplitude $B_{sh}(\alpha)$ and ignoring macroscopic surface roughness, Eq. (8) can be used to express $f(\alpha)$, and the HG lunar–Lambert function can be written as

$$I(\mu, \mu_0, \alpha)/F = A\left\{\big(1 - \zeta^2\big)/\big(1 + 2\zeta\cos(\alpha) + \zeta^2\big)^{3/2}\right\}$$
$$\times \left\{1 + B_{so}\big(1 + (1/h_s)\tan(\alpha/2)\big)^{-1}\right\}$$
$$\times \big(\mu_0/(\mu + \mu_0)\big) + B\mu_0. \qquad (11)$$

For the purposes of this paper, Eq. (11) will be referred to as the "HG lunar–Lambert function."

3.4. Hapke function

Hapke's (1981, 1993, 2002) photometric model has been shown to accurately fit data from a wide variety of planetary surfaces and laboratory samples (e.g., Guinness, 1981; Helfenstein and Veverka, 1987; Arvidson et al., 1989; Domingue and Hapke, 1992; Hillier et al., 1994; Helfenstein et al., 1996; Domingue et al., 1997; Guinness et al., 1997; Helfenstein et al., 1997; Johnson et al., 1999, 2006). Ignoring terms for macroscopic roughness and the CBOE, Hapke's equation can be written as:

$$I(\mu, \mu_0, \alpha)/F = (w/4)\big(\mu_0/(\mu + \mu_0)\big)$$
$$\times \big[p(\alpha)B_{sh}(\alpha) + M(\mu, \mu_0)\big], \qquad (12)$$

where $M(\mu, \mu_0)$ is the multiple-scattering term defined by Eq. (17) of Hapke (2002) and w is the single-scattering albedo. Using the HG function given in Eq. (9) to describe $p(\alpha)$ and Hapke's expression for the SHOE given by Eq. (10) for $B_{sh}(\alpha)$ the Hapke function can be written as

$$I(\mu, \mu_0, \alpha)/F$$
$$= (w/4)\big(\mu_0/(\mu + \mu_0)\big)$$

$$\times \left[\left\{ (1 - \zeta^2)/(1 + 2\zeta \cos(\alpha) + \zeta^2)^{3/2} \right\} \right.$$
$$\left. \times \left\{ 1 + B_{so}(1 + (1/h_s)\tan(\alpha/2))^{-1} \right\} + M(\mu, \mu_0) \right]. \quad (13)$$

3.5. Modeling approach

In order to develop an adequate model of the martian surface photometric function with the fewest variables/complexities, we fit our data to five photometric functions: a "Lambert function" (Eq. (1)), a "Minnaert function" (Eq. (2)), the "empirical lunar–Lambert function" (Eq. (7)), the "HG lunar–Lambert function" (Eq. (11)), and a "Hapke function" (Eq. (13)) for the various bins described in Section 2. Binned data were fit to functions using a Levenberg–Marquardt non-linear least squares program (Levenberg, 1944; Marquardt, 1963) to minimize chi-squared (χ^2) defined as

$$\chi^2 = \sum_i \left[(I/F_{i \text{ modeled}} - I/F_{i \text{ observed}})/\sigma_i \right]^2,$$

where σ_i is the error in $I/F_{i \text{ observed}}$. Dividing χ^2 by the number of degrees of freedom (DOF) gives the reduced chi-squared (χ_ν^2), a measure of the goodness-of-fit. χ_ν^2 is used to evaluate and statistically compare the various models and binning criteria discussed above.

Plots of observed reflectance versus modeled reflectance were also used as a visual aid in determining the goodness of fit. An ideal model will yield reflectance identical to that observed for each data point and would therefore plot along a line of $I/F_{\text{modeled}} = I/F_{\text{observed}}$. In these plots, scatter around a line of $I/F_{\text{modeled}} = I/F_{\text{observed}}$ results from a normal distribution of the data; clusters of points away from this line are indicative of problems with the fit, either in the model function or in the criteria used to bin the data. Such plots allow statistically comparable fits with similar χ_ν^2 values to be compared in order to identify the superior fit.

4. Results

HST WFPC2 data acquired at 502, 673, 953, and 1042 nm were sorted into Viking bolometric albedo bins, TES bolometric albedo bins, TES thermal inertia bins, and historic geographic units (shown in Figs. 2 through 5) and were fit to five photometric functions described in detail above. Fig. 10 shows the χ_ν^2 goodness of fit for fits to these scattering functions plotted against the different binning criteria. For all five scattering models the best fits were achieved by binning the data into geographic units. This result is not surprising, however, considering the spatial extent of each these geographic unit is small compared to the global extent of the other bins discussed. Tables 3, 5, 7, 9, and 11 list by scattering model the fits to the geographic units shown in Fig. 5. All model fits include the best-fit model parameters with associated errors computed from the covariance matrix weighted by χ_ν^2, the χ_ν^2 estimate of their goodness of fit, and the number of DOF. Parameters underconstrained in a model are indicated by reporting '- - -' for the error. These results for specific photometric models are discussed in greater detail in the following sections.

In Fig. 10 it is seen that for all five photometric models considered, data sorted by TES bolometric albedo have the lowest χ_ν^2 values among the three global binning criteria (Viking IRTM and TES bolometric albedos and TES TI). The χ_ν^2 values are useful in identifying statistically better fits by measuring the magnitude that the modeled data deviate from the observed data. However this parameter provides no information about the manner in which the modeled data deviate from the observed data. A useful technique to examine the fit further is to plot observed data against modeled data for the various model fits. Data modeled perfectly will follow a one-to-one line. Scatter about a line of slope one ($I/F_{\text{modeled}} = I/F_{\text{observed}}$) is the result of the normal distribution of the data and will contribute to an increase in χ_ν^2. Trends or clusters of data points away from the line $I/F_{\text{modeled}} = I/F_{\text{observed}}$ also contribute to an increase in χ_ν^2; however, these trends indicate poor model fits.

Figs. 11–15 show examples of such error plots for the five photometric functions; each figure contains four frames: data modeled for three TES albedo bins, for three Viking IRTM albedo bins, for three TES TI bins, and for four geographic regions. By comparing the values of χ_ν^2 plotted in Fig. 10 as well as the values of χ_ν^2 calculated for individual bins of data and visually inspecting the error plots like those shown in Figs. 11–15, it was determined that the best fits are achieved when the data are binned into TES bolometric albedo bins.

In Fig. 10b we can compare the model fits for different sized TES bolometric albedo bins. We see that for all five photometric functions the two statistically best fits are achieved when the modeled data are binned into three and five TES albedo bins. A comparison of scatter plots similar to those shown in Figs. 11–15 using five bins instead of three confirms that these two fits are comparable. Remaining consistent with the goal of this study to produce a simple accurate photometric model, more weight is given to models with fewer numbers of bins. Thus, the preferred solution is achieved when modeled data are sorted according to TES bolometric albedo into three bins equal in size and regularly spaced. A map of these bins is shown in Fig. 3b.

Tables 4, 6, 8, 10, and 12 provide parameters fits from model solution for the five photometric functions discussed in Section 3 fit globally as well as to data from three TES bolometric albedo bins. All model fits include the best-fit model parameters with associated errors, the χ_ν^2 estimate of their goodness of fit, and the number of DOF. Underconstrained parameters are indicated by reporting '- - -' for the error. Results for the individual photometric functions are discussed below.

4.1. Lambert function

The Lambert function given in Eq. (1) is a simple analytic function describing the scattering of a diffuse surface, depending only on the incidence angle. Parameters from representative fits to the Lambert function are presented in Tables 3 and 4. Table 3 lists the parameters from fits to data from the geographic regions; Table 4 provides parameters for a global fit and for data sorted by TES bolometric albedo into three bins. While the Lambert albedo (A_L) shows a strong correlation with bolo-
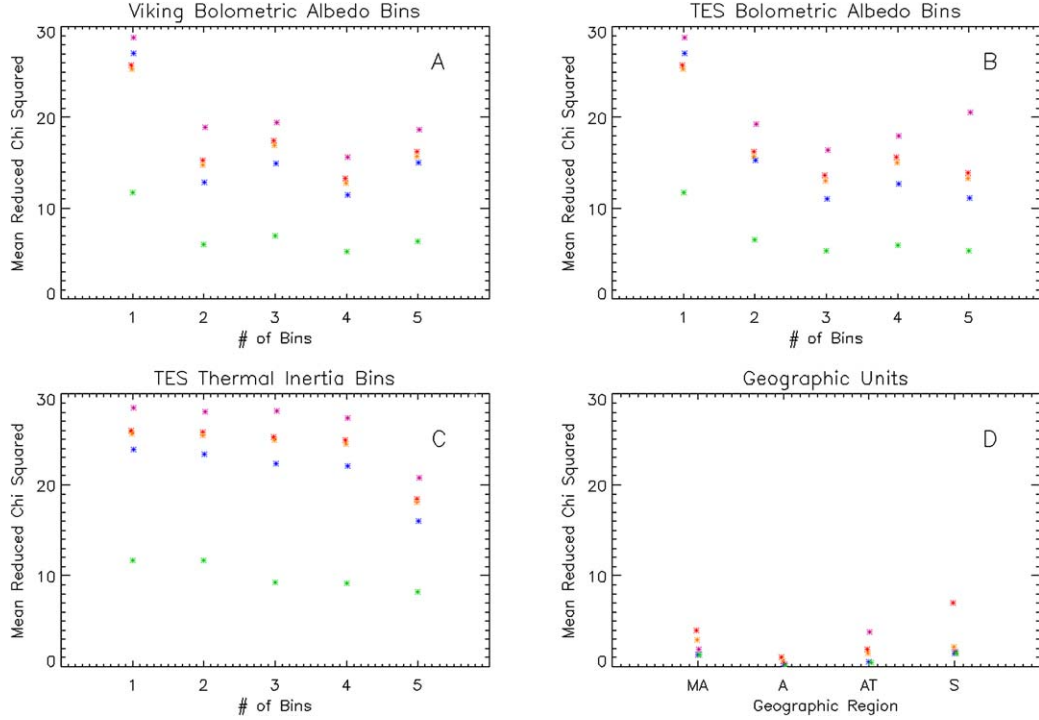
Fig. 10. χ_ν^2 values plotted against the number of model bins for the five different photometric functions used in this study. Plotted values are offset in the 'X' direction for clarity. Red = Lambert function, orange = Minnaert function, green = empirical lunar–Lambert function, blue = HG lunar–Lambert function, purple = Hapke function. The four different frames show results from the four different binning criteria used. (A) Data sorted by Viking IRTM bolometric albedo into two to five bins. (B) Data sorted by TES bolometric albedo into two to five bins. (C) Data sorted by TES thermal inertia into two to five bins. (D) Data sorted by geographic regions shown in Fig. 5. Frames A–C include fits to the global data sets ("one bin") for completeness.
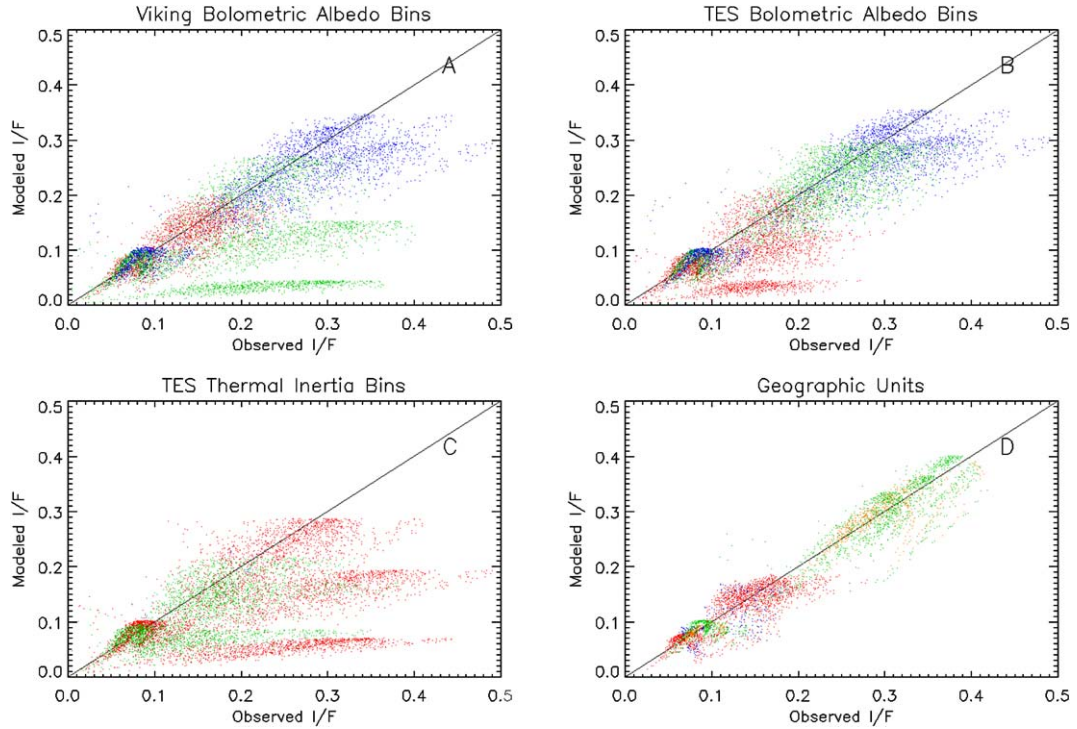
Fig. 11. Observed I/F versus I/F modeled using a Lambert scattering function. The model parameters were derived from data (A) sorted into three Viking IRTM bolometric albedo bins (see Fig. 2B), (B) sorted into three TES bolometric albedo bins (see Fig. 3B), (C) sorted into three TES thermal inertia bins (see Fig. 4B), and (D) binned by geographic region (shown in Fig. 5). Frames A–C data are colored by bin: low bin = red, middle bin = green, and high bin = blue. Frame D data are colored by geographic region: Mare Acidalium = red, Amazonis Planitia = orange, Arabia Terra = green, and Syrtis Major = blue. The clusters of points away from $I/F_{\mathrm{modeled}} = I/F_{\mathrm{observed}}$ show where the Lambert function failed to accurately model the surface reflectance. Of the global binning criteria considered, data binned by TES bolometric albedo yield the best fits to the Lambert function.

Table 3
Lambert scattering parameters for select geographic regions

Region	Parameter	502 nm	673 nm	953 nm	1042 nm
Amazonis Planitia	A_L	0.098 ± 0.001	0.32 ± 0.00	0.36 ± 0.00	0.39 ± 0.00
	χ_ν^2	1.9	0.84	0.73	0.65
	DOF	231	228	208	212
Arabia Terra	A_L	0.10 ± 0.00	0.34 ± 0.00	0.37 ± 0.00	0.40 ± 0.00
	χ_ν^2	3.1	1.1	1.5	1.5
	DOF	518	509	366	432
Mare Acidalium	A_L	0.082 ± 0.001	0.18 ± 0.00	0.17 ± 0.00	0.19 ± 0.01
	χ_ν^2	4.7	3.7	3.5	3.8
	DOF	512	511	406	459
Syrtis Major	A_L	0.091 ± 0.003	0.17 ± 0.00	0.13 ± 0.00	0.16 ± 0.01
	χ_ν^2	8.2	8.8	2.8	6.0
	DOF	73	73	40	57

Table 4
Lambert scattering parameters for data sorted by TES bolometric albedo

TES Albedo	Parameter	502 nm	673 nm	953 nm	1042 nm
0.11–0.31	A_L	0.10 ± 0.00	0.26 ± 0.00	0.079 ± 0.003	0.19 ± 0.00
	χ_ν^2	4.8	6.4	68	34
	DOF	2360	2350	1816	2134
0.11–0.18	A_L	0.097 ± 0.001	0.21 ± 0.00	0.046 ± 0.003	0.14 ± 0.00
	χ_ν^2	5.4	5.1	74	36
	DOF	881	876	649	780
0.18–0.24	A_L	0.10 ± 0.00	0.29 ± 0.00	0.30 ± 0.00	0.29 ± 0.00
	χ_ν^2	4.9	2.8	2.9	11
	DOF	838	835	643	765
0.24–0.31	A_L	0.10 ± 0.00	0.33 ± 0.00	0.36 ± 0.00	0.31 ± 0.01
	χ_ν^2	3.5	1.5	2.2	19
	DOF	639	637	522	587

metric albedo at 673, 953, and 1042 nm, A_L is seen to be low and relatively insensitive to bolometric albedo at 502 nm, consistent with the presence of a strong Fe–O absorption at this (and shorter) wavelengths (Soderblom, 1992; Bell, 1996).

The goodness of the fits to the Lambert model can be assessed by the relatively high values of χ_ν^2 plotted in Fig. 10, suggesting that the scattering properties of the martian surface are not well described by a Lambert function. The plots of observed reflectance versus the Lambert modeled reflectance shown in Fig. 11 showing a high degree of scatter and clusters of points away from the line $I/F_{\mathrm{modeled}} = I/F_{\mathrm{observed}}$ are consistent with this conclusion.

4.2. Minnaert function

The Minnaert function given in Eq. (2) is a generalized form of the Lambert function, which includes a dependence on the emission angle and an empirical parameter. Parameters from representative fits to the Minnaert function are presented in Tables 5 and 6. Table 5 lists the parameters from fits to data from the geographic regions; Table 6 provides parameters for a global fit and for data sorted by TES bolometric albedo into three bins. Unlike A_L, the Minnaert albedo (A_M) is seen to correlate well with bolometric albedo in both the visible and near infrared. Values of k exhibit trends consistent with previous works (e.g., Binder and Jones, 1972; Erard et al., 1994; de Grenier and Pinet, 1995; Bell et al., 1999; Esposito et al.,

2006) with k generally increasing with both wavelength and albedo, though the values of k reported for global fits are systematically higher than values reported for the fits of the smaller geographic regions.

Fits to the Minnaert function appear to be only slightly better than fits to the Lambert function, as is evident by the values of χ_ν^2 reported in Fig. 10 for the two functions. The plots of observed reflectance versus the Minnaert modeled reflectance shown in Fig. 12 showing a high degree of scatter and clusters of points away from the line $I/F_{\mathrm{modeled}} = I/F_{\mathrm{observed}}$ suggest that the scattering parameters of the martian surface are not well modeled by the Minnaert function.

4.3. Empirical lunar–Lambert function

The empirical lunar–Lambert function given in Eq. (7) is an empirical expression of the reflectance of a surface as a linear combination of a Lambert function and a Lommel–Seeliger lunar scattering function. This expression has five empirical free parameters: A, C, D, E, and F. Parameter A describes relative lunar-like and Lambert contributions to the scattering function; $A = 1$ yields a lunar-like function, $A = 0$ a Lambert function. Parameters C, D, E, and F describe the phase dependence of the scattering function. The linear nature of the phase function is empirically described as a line of slope D and intercept C. This term dominates the phase function at higher phase angles. Parameters E and F describe the amplitude and decay rate of

Table 5
Minnaert scattering parameters for select geographic regions

Region	Parameter	502 nm	673 nm	953 nm	1042 nm
Amazonis Planitia	A_M	0.027 ± 0.000	0.091 ± 0.001	0.10 ± 0.00	0.11 ± 0.00
	k	0.42 ± 0.05	0.58 ± 0.03	0.58 ± 0.02	0.71 ± 0.03
	χ_ν^2	1.2	0.41	0.22	0.46
	DOF	230	227	207	211
Arabia Terra	A_M	0.029 ± 0.000	0.10 ± 0.00	0.12 ± 0.00	0.13 ± 0.00
	k	0.70 ± 0.02	0.87 ± 0.01	$1 \pm \text{- - -}$	$1 \pm \text{- - -}$
	χ_ν^2	2.0	0.82	1.5	1.6
	DOF	517	508	365	431
Mare Acidalium	A_M	0.021 ± 0.000	0.049 ± 0.001	0.047 ± 0.001	0.052 ± 0.001
	k	0.58 ± 0.02	0.68 ± 0.02	0.74 ± 0.02	0.73 ± 0.02
	χ_ν^2	3.2	2.7	2.9	3.1
	DOF	511	510	405	458
Syrtis Major	A_M	0.023 ± 0.000	0.044 ± 0.001	0.040 ± 0.001	0.044 ± 0.001
	k	0.52 ± 0.02	0.54 ± 0.03	$1 \pm \text{- - -}$	0.62 ± 0.04
	χ_ν^2	1.4	2.0	2.9	2.7
	DOF	72	72	39	56

Table 6
Minnaert scattering parameters for data sorted by TES bolometric albedo

TES Albedo	Parameter	502 nm	673 nm	953 nm	1042 nm
0.11–0.31	A_M	0.028 ± 0.000	0.077 ± 0.001	0.025 ± 0.001	0.060 ± 0.001
	k	0.77 ± 0.01	0.10 ± 0.01	$1 \pm \text{- - -}$	$1 \pm \text{- - -}$
	χ_ν^2	3.5	6.2	69	34
	DOF	2359	2349	1815	2133
0.11–0.18	A_M	0.026 ± 0.000	0.060 ± 0.001	0.015 ± 0.001	0.043 ± 0.001
	k	0.74 ± 0.01	0.82 ± 0.01	$1 \pm \text{- - -}$	$1 \pm \text{- - -}$
	χ_ν^2	3.5	4.0	74	36
	DOF	880	875	648	779
0.18–0.24	A_M	0.028 ± 0.000	0.084 ± 0.001	0.089 ± 0.001	0.094 ± 0.001
	k	0.71 ± 0.01	0.85 ± 0.01	0.89 ± 0.01	$1 \pm \text{- - -}$
	χ_ν^2	2.9	2.1	2.6	11
	DOF	837	834	642	764
0.24–0.31	A_M	0.031 ± 0.000	0.10 ± 0.00	0.11 ± 0.00	0.098 ± 0.002
	k	0.81 ± 0.01	0.94 ± 0.01	$1 \pm \text{- - -}$	$1 \pm \text{- - -}$
	χ_ν^2	2.8	1.4	2.2	19
	DOF	638	636	521	586

the exponential term in the phase function. These parameters describe any non-linear surge in reflectance below ∼20°. Parameters from representative fits to the empirical lunar–Lambert function are presented in Tables 7 and 8. Table 7 lists the parameters from fits to data from the geographic regions; Table 8 provides parameters for a global fit and for data sorted by TES bolometric albedo into three bins.

Parameter A is well constrained by all the fits and exhibits an inverse relationship with bolometric albedo, implying that the martian surface is less lunar like and slightly more Lambertian at higher albedos. This is consistent with the fact that Lambert's law is a better approximation of the reflectance of high-albedo surfaces (Hapke, 1993), and that the Lommel–Seeliger lunar function provides a better model for the reflectance of low-albedo surfaces (Hapke, 1993). A also exhibits an inverse relationship with wavelength, but because the values of χ_ν^2 are larger at longer wavelengths this is interpreted primarily as an indication that the surface reflectance is less well defined by the Lommel–Seeliger lunar function and not as an indication that the martian surface scatters more diffusely at longer wavelengths.

The parameters associated with the empirical scattering function $f(\alpha)$, though not as well constrained as A given the available phase coverage, can provide some constraints on the surface physical properties. The magnitude E of the exponential term is related to the amplitude of the opposition peak. The amplitude of the opposition peak is related to the opacity of the scattering particles, with more opaque particles exhibiting larger opposition peaks (Hapke, 1986, 1993). The exponential decay rate F is inversely related to the angular width of the opposition peak. The angular width of the opposition peak is related to the particle size distribution and surface packing density, with narrow opposition peaks defined by larger decay rates (larger values of F) corresponding to more loosely packed surfaces and/or non-uniform grain size distributions (Hapke, 1986, 1993). Though poor phase coverage from ∼15° to 30° and no data above 40° limited the model's ability to separate the linear and exponential terms of the scattering function, our results suggest that the scattering particles are more opaque and less closely-packed particles and/or have a less uniform grain size distribution at higher bolometric albedos.

Table 7
Empirical lunar–Lambert scattering parameters for select geographic regions

Region	Parameter	502 nm	673 nm	953 nm	1042 nm
Amazonis Planitia	A	0.99 ± 0.00	0.89 ± 0.01	0.85 ± 0.01	0.81 ± 0.02
	C	0.14 ± 0.01	0.36 ± 0.01	0.40 ± 0.01	0.39 ± 0.03
	D	$0 \pm \text{- - -}$	$0 \pm \text{- - -}$	$0 \pm \text{- - -}$	$0 \pm \text{- - -}$
	E	0.13 ± 0.01	0.23 ± 0.01	0.23 ± 0.01	0.32 ± 0.04
	F	0.079 ± 0.007	0.069 ± 0.007	0.090 ± 0.010	0.097 ± 0.017
	χ_ν^2	0.10	0.036	0.051	0.19
	DOF	227	224	204	208
Arabia Terra	A	0.97 ± 0.00	0.78 ± 0.00	0.62 ± 0.01	0.58 ± 0.00
	C	0.15 ± 0.00	0.35 ± 0.01	0.22 ± 0.02	0.23 ± 0.02
	D	$-0.00091 \pm 8\text{E}{-5}$	-0.0038 ± 0.0001	-0.0074 ± 0.0005	-0.0085 ± 0.0003
	E	0.15 ± 0.01	0.32 ± 0.05	$0 \pm \text{- - -}$	$0 \pm \text{- - -}$
	F	0.22 ± 0.02	0.37 ± 0.05	$0 \pm \text{- - -}$	$0 \pm \text{- - -}$
	χ_ν^2	0.20	0.082	0.94	0.59
	DOF	514	505	362	428
Mare Acidalium	A	0.98 ± 0.00	0.91 ± 0.01	0.89 ± 0.01	0.88 ± 0.01
	C	0.073 ± 0.004	0.25 ± 0.01	0.19 ± 0.01	0.19 ± 0.01
	D	$0 \pm \text{- - -}$	-0.0030 ± 0.0001	-0.0028 ± 0.0002	-0.0029 ± 0.0002
	E	0.10 ± 0.00	$0 \pm \text{- - -}$	$0 \pm \text{- - -}$	$0 \pm \text{- - -}$
	F	0.064 ± 0.005	$0 \pm \text{- - -}$	$0 \pm \text{- - -}$	$0 \pm \text{- - -}$
	χ_ν^2	0.67	1.2	1.7	1.7
	DOF	508	507	402	455
Syrtis Major	A	0.98 ± 0.00	0.96 ± 0.01	0.93 ± 0.05	0.94 ± 0.01
	C	0.14 ± 0.00	0.26 ± 0.01	0.14 ± 0.11	0.21 ± 0.02
	D	$-0.0012 \pm 9\text{E}{-5}$	-0.0018 ± 0.0003	-0.0011 ± 0.0005	-0.0013 ± 0.0004
	E	$0 \pm \text{- - -}$	$0 \pm \text{- - -}$	$0 \pm \text{- - -}$	$0 \pm \text{- - -}$
	F	$0 \pm \text{- - -}$	$0 \pm \text{- - -}$	$0 \pm \text{- - -}$	$0 \pm \text{- - -}$
	χ_ν^2	0.35	1.4	2.8	2.2
	DOF	69	69	36	53

Table 8
Empirical lunar–Lambert scattering parameters for data sorted by TES bolometric albedo

| TES Albedo	Parameter	502 nm	673 nm	953 nm	1042 nm
0.11–0.31	A	0.96 ± 0.00	0.80 ± 0.00	0.65 ± 0.01	0.64 ± 0.01
	C	$0.11 \pm \text{- - -}$	$0.22 \pm \text{- - -}$	$0 \pm \text{- - -}$	$0 \pm \text{- - -}$
	D	$-0.00091 \pm 1.3\text{E}{-4}$	-0.0039 ± 0.0017	-0.011 ± 0.000	-0.0089 ± 0.0003
	E	0.097 ± 0.004	$0 \pm \text{- - -}$	$0 \pm \text{- - -}$	$0 \pm \text{- - -}$
	F	0.036 ± 0.002	$0 \pm \text{- - -}$	$0 \pm \text{- - -}$	$0 \pm \text{- - -}$
	χ_ν^2	1.1	4.9	28	18
	DOF	2356	2346	1812	2130
0.11–0.18	A	0.97 ± 0.00	0.89 ± 0.00	0.74 ± 0.01	0.73 ± 0.01
	C	0.10 ± 0.02	0.26 ± 0.01	$0 \pm \text{- - -}$	$0 \pm \text{- - -}$
	D	$-0.00064 \pm 3.4\text{E}{-4}$	-0.0034 ± 0.0001	-0.0073 ± 0.0003	-0.0062 ± 0.0004
	E	0.072 ± 0.012	$0 \pm \text{- - -}$	$0 \pm \text{- - -}$	0.079 ± 0.050
	F	0.092 ± 0.026	$0 \pm \text{- - -}$	$0 \pm \text{- - -}$	0.11 ± 0.11
	χ_ν^2	0.82	2.0	32	18
	DOF	877	872	645	776
0.18–0.24	A	0.96 ± 0.00	0.78 ± 0.00	0.79 ± 0.01	0.61 ± 0.01
	C	0.15 ± 0.00	0.18 ± 0.02	0.31 ± 0.01	0.094 ± 0.018
	D	-0.0019 ± 0.0000	-0.0020 ± 0.0006	-0.0050 ± 0.0002	-0.0096 ± 0.0004
	E	$0 \pm \text{- - -}$	0.25 ± 0.02	$0 \pm \text{- - -}$	$0 \pm \text{- - -}$
	F	$0 \pm \text{- - -}$	0.28 ± 0.05	$0 \pm \text{- - -}$	$0 \pm \text{- - -}$
	χ_ν^2	0.74	0.95	1.5	4.4
	DOF	834	831	639	761
0.24–0.31	A	0.96 ± 0.00	0.75 ± 0.00	0.62 ± 0.01	0.49 ± 0.00
	C	0.12 ± 0.00	0.27 ± 0.01	$0 \pm \text{- - -}$	$0 \pm \text{- - -}$
	D	-0.0011 ± 0.0002	-0.0040 ± 0.0003	-0.0025 ± 0.0004	-0.015 ± 0.000
	E	0.13 ± 0.01	0.37 ± 0.11	0.29 ± 0.04	$0 \pm \text{- - -}$
	F	0.19 ± 0.03	0.36 ± 0.12	0.12 ± 0.03	$0 \pm \text{- - -}$
	χ_ν^2	0.45	0.41	1.3	3.4
	DOF	635	633	518	583
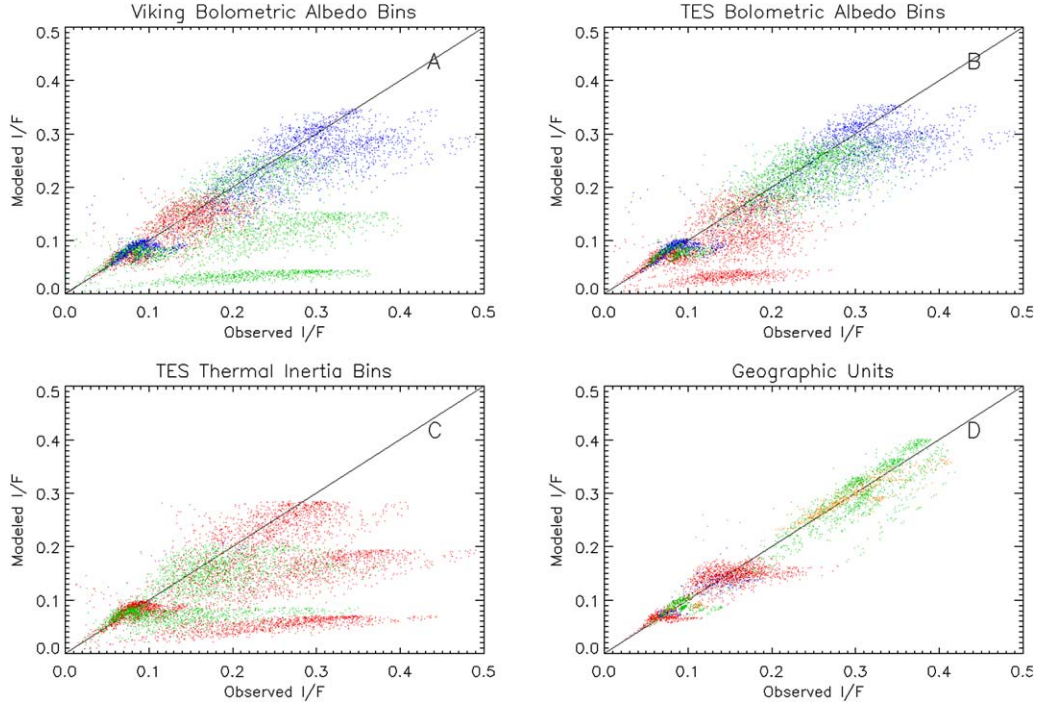
Fig. 12. Observed I/F versus I/F modeled using a Minnaert scattering function. The model parameters were derived from data (A) sorted into three Viking IRTM bolometric albedo bins (see Fig. 2B), (B) sorted into three TES bolometric albedo bins (see Fig. 3B), (C) sorted into three TES thermal inertia bins (see Fig. 4B), and (D) binned by geographic region (shown in Fig. 5). Frames A–C data are colored by bin: low bin = red, middle bin = green, and high bin = blue. Frame D data are colored by geographic region: Mare Acidalium = red, Amazonis Planitia = orange, Arabia Terra = green, and Syrtis Major = blue. The results from the Minnaert modeling show an improvement over the Lambert modeling but still show clusters of data away from the ideal $I/F_{modeled} = I/F_{observed}$ line where the model broke down. Of the global binning criteria considered, data binned by TES bolometric albedo yield the best fits to the Minnaert function.
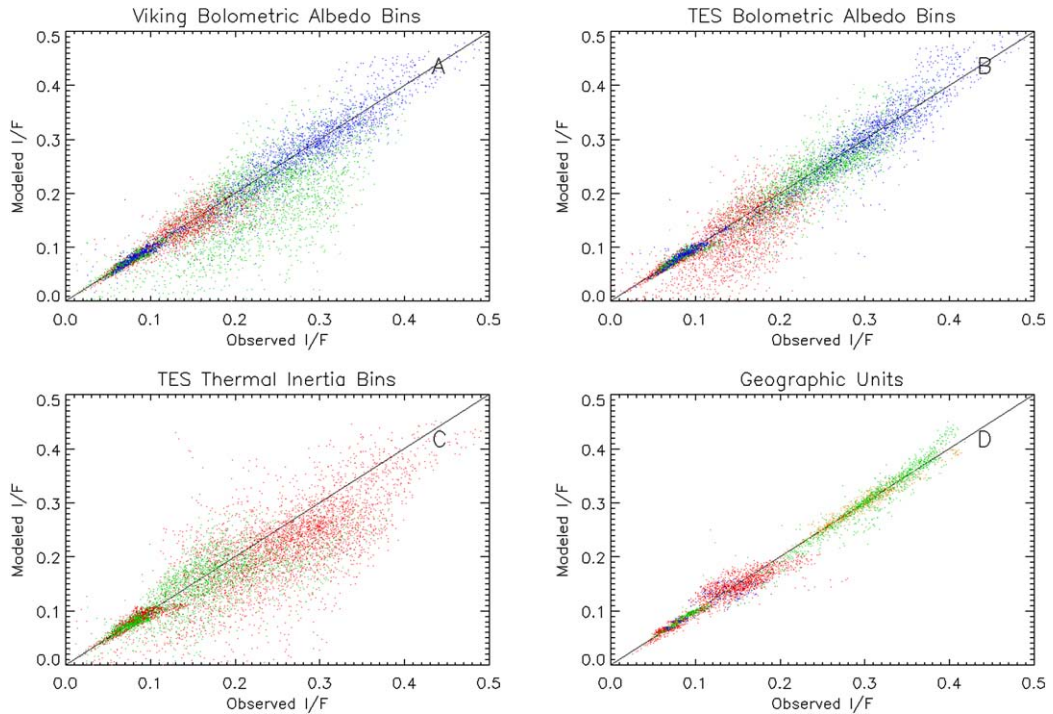

Fig. 13. Observed I/F versus I/F modeled using the empirical lunar–Lambert scattering function. The model parameters were derived from data (A) sorted into three Viking IRTM bolometric albedo bins (see Fig. 2B), (B) sorted into three TES bolometric albedo bins (see Fig. 3B), (C) sorted into three TES thermal inertia bins (see Fig. 4B), and (D) binned by geographic region (shown in Fig. 5). Frames A–C data are colored by bin: low bin = red, middle bin = green, and high bin = blue. Frame D data are colored by geographic region: Mare Acidalium = red, Amazonis Planitia = orange, Arabia Terra = green, and Syrtis Major = blue. The empirical lunar–Lambert scattering function yields the best fits for the data from all five of the photometric functions considered. Of the global binning criteria considered, data binned by TES bolometric albedo yield the best fits to the empirical lunar–Lambert function.

Table 9
HG lunar–Lambert scattering parameters for select geographic regions

Region	Parameter	502 nm	673 nm	953 nm	1042 nm
Amazonis Planitia	A	0.10 ± 0.01	0.27 ± 0.01	0.37 ± 0.04	0.35 ± 0.06
	B	0.0035 ± 0.0034	0.11 ± 0.01	0.14 ± 0.01	0.16 ± 0.02
	ζ	-0.096 ± 0.020	-0.0035 ± 0.0140	0.10 ± 0.03	-0.053 ± 0.052
	B_{so}	$1 \pm \text{- - -}$	$1 \pm \text{- - -}$	$1 \pm \text{- - -}$	$1 \pm \text{- - -}$
	h_s	0.093 ± 0.025	0.13 ± 0.02	0.11 ± 0.02	0.097 ± 0.048
	χ_ν^2	0.12	0.038	0.052	0.20
	DOF	227	224	204	208
Arabia Terra	A	0.077 ± 0.003	0.084 ± 0.003	0.0059 ± 0.0069	0.0062 ± 0.0035
	B	0.020 ± 0.002	0.21 ± 0.00	0.34 ± 0.01	0.37 ± 0.01
	ζ	-0.17 ± 0.03	-0.29 ± 0.02	-0.69 ± 0.13	-0.70 ± 0.06
	B_{so}	$1 \pm \text{- - -}$	$1 \pm \text{- - -}$	$1 \pm \text{- - -}$	$1 \pm \text{- - -}$
	h_s	0.038 ± 0.015	0.027 ± 0.010	$0.37 \pm \text{- - -}$	0.16 ± 0.34
	χ_ν^2	0.28	0.093	1.0	0.89
	DOF	514	505	362	428
Mare Acidalium	A	0.044 ± 0.003	0.059 ± 0.006	0.029 ± 0.027	0.030 ± 0.005
	B	0.022 ± 0.002	0.091 ± 0.005	0.11 ± 0.01	0.13 ± 0.01
	ζ	-0.24 ± 0.03	-0.26 ± 0.03	-0.38 ± 0.34	-0.42 ± 0.04
	B_{so}	$1 \pm \text{- - -}$	$1 \pm \text{- - -}$	0.87 ± 0.92	$1 \pm \text{- - -}$
	h_s	0.044 ± 0.023	0.057 ± 0.032	0.041 ± 0.692	0.012 ± 0.008
	χ_ν^2	0.69	1.1	1.7	1.7
	DOF	508	507	402	455
Syrtis Major	A	0.053 ± 0.012	0.10 ± 0.02	0.061 ± 0.064	0.087 ± 0.023
	B	0.021 ± 0.006	0.042 ± 0.009	0.061 ± 0.054	0.060 ± 0.013
	ζ	-0.26 ± 0.07	-0.26 ± 0.04	-0.27 ± 0.11	-0.24 ± 0.06
	B_{so}	$1 \pm \text{- - -}$	$0 \pm \text{- - -}$	$0 \pm \text{- - -}$	$0 \pm \text{- - -}$
	h_s	0.0043 ± 0.0076	$0 \pm \text{- - -}$	$0 \pm \text{- - -}$	$0 \pm \text{- - -}$
	χ_ν^2	0.35	1.3	2.8	2.1
	DOF	69	69	36	53

Table 10
HG lunar–Lambert scattering parameters for data sorted by TES bolometric albedo

TES Albedo	Parameter	502 nm	673 nm	953 nm	1042 nm
0.11–0.31	A	0.034 ± 0.001	0.022 ± 0.004	$0 \pm \text{- - -}$	0.046 ± 0.001
	B	0.043 ± 0.001	0.20 ± 0.00	0.079 ± 0.003	0.00 ± 0.00
	ζ	-0.31 ± 0.03	-0.48 ± 0.09	$0 \pm \text{- - -}$	-0.60 ± 0.01
	B_{so}	$1 \pm \text{- - -}$	$1 \pm \text{- - -}$	$0 \pm \text{- - -}$	$0 \pm \text{- - -}$
	h_s	0.036 ± 0.020	0.031 ± 0.105	$0 \pm \text{- - -}$	$0 \pm \text{- - -}$
	χ_ν^2	1.1	4.9	69	44
	DOF	2356	2346	1812	2130
0.11–0.18	A	0.042 ± 0.001	0.055 ± 0.003	$0 \pm \text{- - -}$	0.0067 ± 0.0013
	B	0.029 ± 0.001	0.11 ± 0.00	0.046 ± 0.003	0.11 ± 0.01
	ζ	-0.25 ± 0.02	-0.39 ± 0.01	$0 \pm \text{- - -}$	-0.80 ± 0.02
	B_{so}	$1 \pm \text{- - -}$	$1 \pm \text{- - -}$	$0 \pm \text{- - -}$	$0 \pm \text{- - -}$
	h_s	0.050 ± 0.019	0.0048 ± 0.0022	$0 \pm \text{- - -}$	$0 \pm \text{- - -}$
	χ_ν^2	0.83	2.0	75	29
	DOF	877	872	645	776
0.18–0.24	A	0.031 ± 0.001	0.030 ± 0.004	0.036 ± 0.005	0.0031 ± 0.0093
	B	0.045 ± 0.001	0.22 ± 0.00	0.22 ± 0.01	0.26 ± 0.00
	ζ	-0.39 ± 0.03	-0.43 ± 0.07	-0.39 ± 0.02	-0.80 ± 0.23
	B_{so}	0.41 ± 0.09	$1 \pm \text{- - -}$	$1 \pm \text{- - -}$	$1 \pm \text{- - -}$
	h_s	0.029 ± 0.063	0.034 ± 0.074	0.088 ± 0.068	$0.039 \pm \text{- - -}$
	χ_ν^2	0.70	1.0	1.5	9.0
	DOF	834	831	639	761
0.24–0.31	A	0.041 ± 0.002	0.037 ± 0.004	0.0066 ± 0.004	$0 \pm \text{- - -}$
	B	0.041 ± 0.002	0.25 ± 0.00	0.33 ± 0.01	0.31 ± 0.01
	ζ	-0.31 ± 0.04	-0.44 ± 0.06	-0.68 ± 0.04	$0 \pm \text{- - -}$
	B_{so}	$1 \pm \text{- - -}$	$1 \pm \text{- - -}$	$1 \pm \text{- - -}$	$0 \pm \text{- - -}$
	h_s	0.035 ± 0.028	0.031 ± 0.062	0.068 ± 0.141	$0 \pm \text{- - -}$
	χ_ν^2	0.56	0.45	1.5	19
	DOF	635	633	518	583

Despite the limited constraints on some of the empirical parameters in $f(\alpha)$, fits to the empirical lunar–Lambert model do yield statistically the best χ_ν^2 compared with the other photometric functions being considered. Additionally, comparing Fig. 13 with Figs. 11, 12, 14, and 15 shows that the fits to the empirical lunar–Lambert function are qualitatively superior with fewer clusters of data away from the line $I/F_{\text{modeled}} = I/F_{\text{observed}}$ in Fig. 13.

4.4. HG lunar–Lambert function

The HG lunar–Lambert function given in Eq. (11) is similar in form to the empirical lunar–Lambert function previously discussed with the exception of the expression of $f(\alpha)$. For this model $f(\alpha)$ is taken to be the product of a one-term HG function and Hapke's SHOE function. The resulting expression has five parameters: the weighting factors for lunar-like (A) and Lambert (B) terms of the scattering function, the HG cosine asymmetry factor (ζ), and the amplitude (B_{so}) and the angular width (h_s) of the SHOE. Parameters from representative fits to the HG lunar–Lambert function are presented in Tables 9 and 10. Table 9 lists the parameters from fits to data from the geographic regions; Table 10 provides parameters for a global fit and for data sorted by TES bolometric albedo into three bins.

The relative magnitude of A exhibits an inverse relationship with bolometric albedo, suggesting that the higher-albedo martian surface is more Lambertian than the lower-albedo surfaces. This is consistent with what was seen in the empirical lunar–Lambert models and with Hapke's (1993) results that the Lambert's law is a better approximation of the reflectance of high-albedo surfaces and that the Lommel–Seeliger lunar function provides a better approximation for the reflectance of low-albedo surfaces. The relative magnitude of A also exhibits an inverse relationship with wavelength, though as was seen in the empirical lunar–Lambert models the values of χ_ν^2 are larger at longer wavelengths, suggesting that the surface reflectance is less well defined by the Lommel–Seeliger lunar function and not necessarily that the martian surface scatters more diffusely at longer wavelengths.

Most of the surfaces are modeled with a backscattering single-particle phase function indicated by a negative ζ. This result is expected, as these data do not include the high phase angles needed to constrain the forward scattering lobe. Without constraints on the forward scattering nature of the surface we cannot confidently state that any of these surfaces are actually backscattering surfaces and therefore cannot interpret this result in any meaningful manor. The opposition peak described by B_{so} and h_s is not well constrained by any of the fits, though there is some indication that Amazonis Planitia exhibits a more broad opposition peak than Arabia Terra or Mare Acidalium. This would imply that the surface material at Amazonis Planitia is more closely packed and/or of a more uniform grain size distribution (Hapke, 1986, 1993) than other regions.

Values of χ_ν^2 calculated for fits to the HG lunar–Lambert function plotted in Fig. 10 are larger than values of χ_ν^2 reported for the empirical lunar–Lambert function for globally binned data. Data binned into smaller geographic regions, however, are modeled quite well by the HG lunar–Lambert function. Plots of observed reflectance versus the HG lunar–Lambert modeled reflectance shown in Figs. 14A–14C for the globally binned data show clusters of points away from the line $I/F_{\text{modeled}} = I/F_{\text{observed}}$ reminiscent of similar plots for the Lambert and Minnaert fits shown in Figs. 11 and 12, respectively. The global scattering parameters of the martian surface are not well modeled by the HG lunar–Lambert function.

4.5. Hapke function

Equation (13) is an approximated analytic radiative transfer model derived by Hapke (1981, 1993, 2002). This expression of the Hapke function is written in terms of the single-scattering albedo (w), the HG cosine asymmetry factor (ζ), and the amplitude (B_{so}) and the angular extent (h_s) of the SHOE. Parameters from representative fits to the Hapke function are presented in Tables 11 and 12. Table 11 lists the parameters from fits to data from the geographic regions; Table 12 provides parameters for a global fit and for data sorted by TES bolometric albedo into three bins.

Hapke function parameters were well constrained for the four geographic regions and very poorly constrained for the globally binned data. The values of χ_ν^2 plotted in Fig. 10 for the Hapke function are larger than values of χ_ν^2 reported for all of the other functions for globally binned data. The Hapke function did, however, model well the scattering parameters of the data binned into smaller geographic regions. Plots of observed reflectance versus the Hapke modeled reflectance shown in Fig. 15 support the conclusion that while the globally binned data are very poorly modeled by the Hapke function, the scattering properties of the smaller geographic regions are for the most part well described by Hapke's function. Discussion of the parameters constrained by the Hapke model is therefore limited to the fits to the geographic regions.

The best constrained parameter, the single-scattering albedo, shows a strong correlation with bolometric albedo at 673, 953, and 1042 nm with $0.6 < w < 0.7$ for lower-albedo regions and $0.8 < w < 0.9$ for higher albedo regions. Values of single-scattering albedo at 502 nm are relatively insensitive to bolometric albedo, with $w \sim 0.35$. These single-scattering albedos are consistent with those previously reported by Thorpe (1982), Arvidson et al. (1989), Guinness et al. (1997), and Johnson et al. (1999, 2006). The low value of w at 502 nm is consistent with the presence of a strong Fe–O absorption short ward of $\sim$600 nm (Soderblom, 1992; Bell, 1996).

The other parameters, the HG cosine asymmetry factor and the amplitude and angular width of the SHOE are not as well constrained for these regions. As was seen with the HG lunar–Lambert model, most of the surfaces modeled as predominantly backscattering, though again the data used in this study do not include the high phase coverage needed to constrain well the forward scattering. Values of B_{so} and h_s are not well constrained by these fits to the Hapke function.
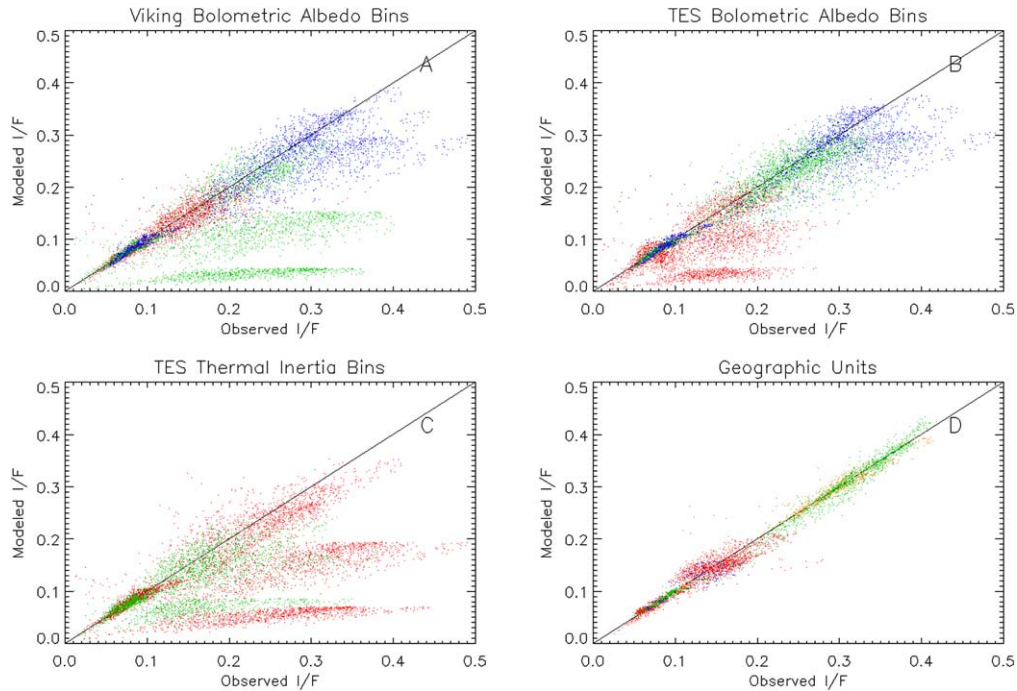
Fig. 14. Observed I/F versus I/F modeled using the HG lunar–Lambert scattering function. The model parameters were derived from data (A) sorted into three Viking IRTM bolometric albedo bins (see Fig. 2B), (B) sorted into three TES bolometric albedo bins (see Fig. 3B), (C) sorted into three TES thermal inertia bins (see Fig. 4B), and (D) binned by geographic region (shown in Fig. 5). Frames A–C data are colored by bin: low bin = red, middle bin = green, and high bin = blue. Frame D data are colored by geographic region: Mare Acidalium = red, Amazonis Planitia = orange, Arabia Terra = green, and Syrtis Major = blue. Though superior to fit to the other functions, the fits to the HG lunar–Lambert function are not as good as those of the empirical lunar–Lambert function as is evidenced by the clusters of data points away from $I/F_{modeled} = I/F_{observed}$. Of the global binning criteria considered, data binned by TES bolometric albedo yield the best fits to the HG lunar–Lambert function.
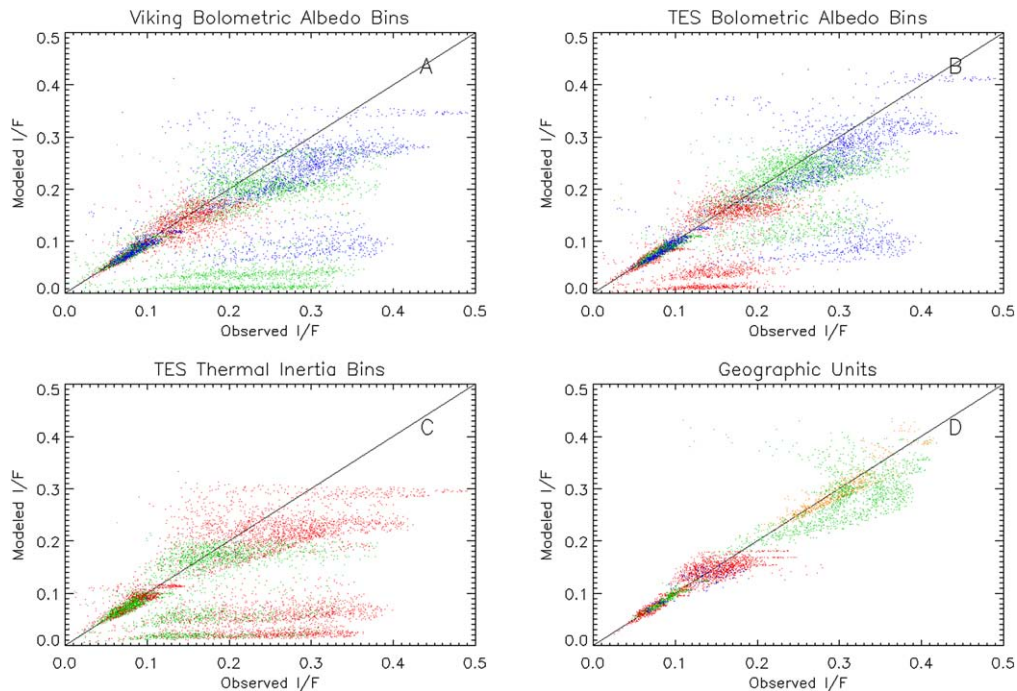

Fig. 15. Observed I/F versus I/F modeled with a Hapke scattering function. The model parameters were derived from data (A) sorted into three Viking IRTM bolometric albedo bins (see Fig. 2B), (B) sorted into three TES bolometric albedo bins (see Fig. 3B), (C) sorted into three TES thermal inertia bins (see Fig. 4B), and (D) binned by geographic region (shown in Fig. 5). Frames A–C data are colored by bin: low bin = red, middle bin = green, and high bin = blue. Frame D data are colored by geographic region: Mare Acidalium = red, Amazonis Planitia = orange, Arabia Terra = green, and Syrtis Major = blue. The fits to the Hapke function show a higher sensitivity to inappropriately binned data than the other models as is seen by the larger contrast in the goodness of the fits between the different binning criteria. Of the global binning criteria considered, data binned by TES bolometric albedo yield the best fits to the Hapke function.

Table 11
Hapke scattering parameters for select geographic regions

Region	Parameter	502 nm	673 nm	953 nm	1042 nm
Amazonis Planitia	w	0.35 ± 0.01	0.84 ± 0.01	0.93 ± 0.03	0.94 ± 0.03
	ζ	-0.13 ± 0.01	-0.082 ± 0.01	-0.079 ± 0.02	-0.13 ± 0.01
	B_{so}	$1 \pm$ - - -	$1 \pm$ - - -	$1 \pm$ - - -	$1 \pm$ - - -
	h_s	0.091 ± 0.022	$0.5 \pm$ - - -	$0.5 \pm$ - - -	$0.5 \pm$ - - -
	χ_v^2	0.13	0.12	0.31	0.46
	DOF	228	225	205	209
Arabia Terra	w	0.36 ± 0.00	0.82 ± 0.06	0.89 ± 0.09	0.81 ± 0.13
	ζ	-0.13 ± 0.02	-0.092 ± 0.03	0.0024 ± 0.085	-0.17 ± 0.04
	B_{so}	$1 \pm$ - - -	$1 \pm$ - - -	$1 \pm$ - - -	$1 \pm$ - - -
	h_s	0.046 ± 0.015	0.31 ± 0.13	$0.5 \pm$ - - -	0.22 ± 0.21
	χ_v^2	0.35	1.3	6.9	8.4
	DOF	515	506	363	429
Mare Acidalium	w	0.27 ± 0.01	0.60 ± 0.03	0.70 ± 0.05	0.72 ± 0.04
	ζ	-0.14 ± 0.01	-0.021 ± 0.016	0.19 ± 0.03	0.16 ± 0.03
	B_{so}	$1 \pm$ - - -	$1 \pm$ - - -	$1 \pm$ - - -	$1 \pm$ - - -
	h_s	0.068 ± 0.017	0.12 ± 0.04	0.088 ± 0.111	0.11 ± 0.08
	χ_v^2	0.84	1.7	2.6	2.7
	DOF	509	508	403	456
Syrtis Major	w	0.38 ± 0.03	0.55 ± 0.03	0.46 ± 0.03	0.70 ± 0.10
	ζ	0.0091 ± 0.2309	-0.17 ± 0.03	-0.23 ± 0.04	0.21 ± 0.11
	B_{so}	$1 \pm$ - - -	$0 \pm$ - - -	$0 \pm$ - - -	$1 \pm$ - - -
	h_s	0.062 ± 0.197	$0 \pm$ - - -	$0 \pm$ - - -	0.12 ± 0.39
	χ_v^2	0.42	1.6	2.8	2.4
	DOF	70	70	37	54

Table 12
Hapke scattering parameters for data sorted by TES bolometric albedo

TES Albedo	Parameter	502 nm	673 nm	953 nm	1042 nm
0.11–0.31	w	0.30 ± 0.00	0.62 ± 0.01	0.045 ± 0.002	0.12 ± 0.003
	ζ	-0.14 ± 0.01	-0.25 ± 0.01	-0.72 ± 0.01	-0.57 ± 0.01
	B_{so}	$1 \pm$ - - -	$0 \pm$ - - -	$1 \pm$ - - -	$1 \pm$ - - -
	h_s	0.014 ± 0.058	$0 \pm$ - - -	$0.5 \pm$ - - -	$0.5 \pm$ - - -
	χ_v^2	1.9	8.8	71	45
	DOF	2357	2347	1813	2131
0.11–0.18	w	0.23 ± 0.00	0.70 ± 0.03	0.029 ± 0.002	0.083 ± 0.004
	ζ	-0.32 ± 0.00	0.45 ± 0.02	-0.74 ± 0.01	-0.60 ± 0.01
	B_{so}	$0 \pm$ - - -	$1 \pm$ - - -	$1 \pm$ - - -	$1 \pm$ - - -
	h_s	$0 \pm$ - - -	0.11 ± 0.15	$0.5 \pm$ - - -	$0.5 \pm$ - - -
	χ_v^2	1.5	2.9	71	41
	DOF	878	873	646	777
0.18–0.24	w	0.32 ± 0.01	0.58 ± 0.03	0.83 ± 0.06	0.29 ± 0.07
	ζ	-0.13 ± 0.02	0.58 ± 0.02	0.017 ± 0.039	-0.40 ± 0.04
	B_{so}	$1 \pm$ - - -	$1 \pm$ - - -	$1 \pm$ - - -	$1 \pm$ - - -
	h_s	0.054 ± 0.019	0.11 ± 0.20	0.15 ± 0.09	0.27 ± 0.35
	χ_v^2	1.2	1.6	4.3	29
	DOF	835	832	640	762
0.24–0.31	w	0.32 ± 0.01	0.82 ± 0.04	0.88 ± 0.12	0.17 ± 0.01
	ζ	-0.19 ± 0.02	-0.12 ± 0.02	-0.053 ± 0.056	-0.60 ± 0.01
	B_{so}	$1 \pm$ - - -	$1 \pm$ - - -	$1 \pm$ - - -	$1 \pm$ - - -
	h_s	0.047 ± 0.021	0.13 ± 0.05	0.15 ± 0.13	$0.5 \pm$ - - -
	χ_v^2	1.1	3.0	9.5	43
	DOF	636	634	519	584

5. Conclusions and implications

We have modeled the scattering properties of the martian surface using a variety of photometric functions for a variety of surface types. Our preferred photometric model is the empirical lunar–Lambert function given in Eq. (7), fit to three surface regions defined by TES bolometric albedo as low-, moderate-, and high-albedo surfaces, and valid under periods of low atmospheric opacity ($\tau < 0.5$) and for phase angles of $2.7° < \alpha < 40°$. The modeled parameters for these three surface types, listed by wavelength, are given in Table 8.

Studies conducted recently (e.g., Bell et al., 1999; Geissler, 2005) have demonstrated that the martian surface has been undergoing constant dramatic changes in albedo over time, including increases/decreases of up to 80% in I/F in some regions (Bell et al., 1999). Such changes are consistent with the HST data presented in this paper correlating better to the TES bolometric albedo maps than to the Viking IRTM bolometric albedo maps. The poor correlation between the TES TI maps constructed from data acquired in the thermal infrared and the visible to near-infrared scattering properties of the martian surface may be a manifestation of the different skin depths of the two measurements; visible and near-infrared scattering properties are only sensitive to the uppermost few microns of the surface, while TI measurements can be sensitive to depths of order centimeters.

The parameters fit to the empirical lunar–Lambert function suggest that the scattering properties of the martian surface are less lunar like and more Lambert like at higher albedos. This is consistent with the fact that the Lommel–Seeliger lunar function provides a better model for the reflectance of low-albedo surfaces and Lambert's law is a better approximation of the reflectance of high-albedo surfaces (Hapke, 1993). The martian surface is modeled to be less lunar like and more Lambertian at longer wavelengths. As the fits at these longer wavelengths are seen to be poorer, this is interpreted as an indication that the reflectance of the martian surface is less well defined by the Lommel–Seeliger lunar function at longer wavelengths. Though the model's ability to separate the linear and exponential terms of the scattering function $f(\alpha)$ is limited due to the available phase coverage, the fitted parameters indicate that the scattering particles that comprise the high-albedo surfaces are more opaque and more loosely packed particles and/or have a non-uniform grain size distribution compared to lower-albedo surfaces. This is consistent with the high-albedo surfaces being dustier than the low-albedo surfaces.

Other models considered in this study included a Minnaert function, a Lambert function, a HG lunar–Lambert function, and a Hapke function. Fig. 16 shows example solutions

for these four photometric functions and the empirical lunar–Lambert function fit to the 502 nm data from the high-albedo bin of a three-bin TES bolometric albedo map; two frames show examples of data with low incidence (i) and emission (e) angles and high i and e angles. Fits to the Lambert function and the Minnaert function are seen to be quite poor at high i and e. The Minnaert function has been shown in previous studies to be inadequate for broad ranges of i, e, and α (e.g., Veverka et al., 1978; Goguen, 1981; McEwen, 1991) and breaks down entirely near the limb (Hapke, 1993; Bell et al., 1999). As the Lambert function can be derived from a Minnaert function by setting $k = 1$ it follows that the Lambert function is subject to the same inadequacies expressed by the Minnaert function. Both the HG lunar–Lambert function and the Hapke function describe the reflectance of the smaller geographic regions reasonably, though neither model produces good fits for the global data. This is particularly evident for Hapke's function, which does a very poor job describing the scattering properties of large regions. Despite the relatively poor fits of these four photometric functions, some information can be gained from the parameters fit to these models.

The Lambert albedo is strongly correlates with bolometric albedo at 673, 953, and 1042 nm. At 502 nm the Lambert albedo is low and does not vary with bolometric albedo, consistent with the presence of a strong Fe–O absorption at this (and shorter) wavelengths (Soderblom, 1992; Bell, 1996). The Minnaert albedo correlates with bolometric albedo in both the visible and near infrared. The Minnaert index increases with both albedo and wavelength, consistent with previous works (e.g., Binder and Jones, 1972; Erard et al., 1994; de Grenier and Pinet, 1995; Esposito et al., 2006).

Fits to the HG lunar–Lambert function indicate that the martian surface is less lunar like and more Lambertian at higher-bolometric albedos. This same trend was noted in the empirical lunar–Lambert models and is consistent with Lambert's law better describing of the reflectance of high-albedo surfaces and the Lommel–Seeliger lunar function better describing the reflectance of low-albedo surfaces (Hapke, 1993). Though not
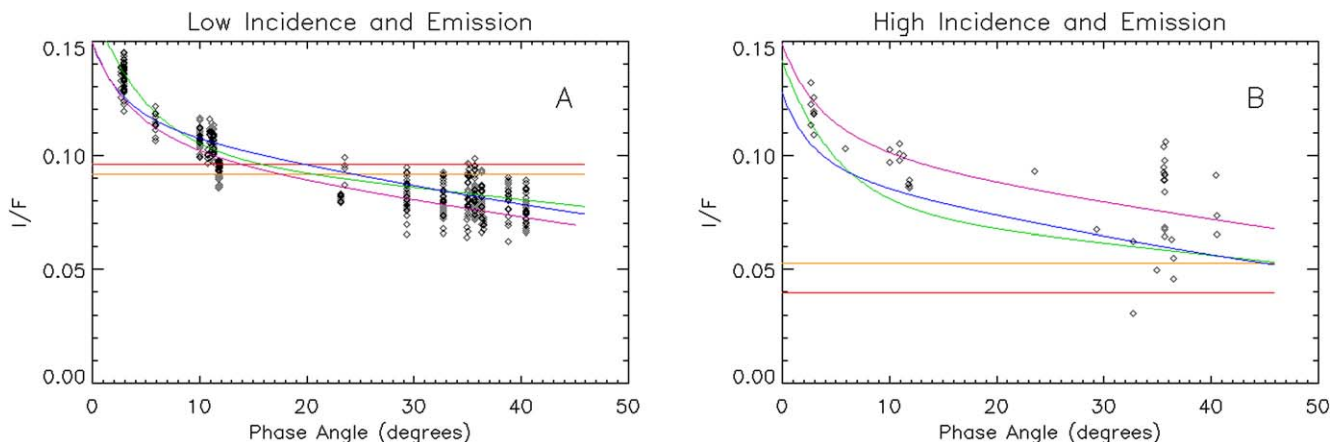

Fig. 16. I/F versus phase for 502 nm data from the high-albedo bin of the three-bin TES bolometric albedo map shown in Fig. 3B. Solutions to the Lambert function (red), Minnaert function (orange), empirical lunar–Lambert function (green), HG lunar–Lambert function (blue), and Hapke function (purple) for these data are plotted. Examples of low and high i and e are shown in the two frames. (A) Data plotted have $i < 45°$ and $e < 45°$; photometric functions plotted for $i = 22.5°$ and $e = 22.5°$. (B) Data plotted have $i > 45°$ and $e > 45°$; photometric functions plotted for $i = 67.5°$ and $e = 67.5°$.

well constrained by the model, the scattering parameters describing the opposition peak indicate that the surface material of Amazonis Planitia is more closely packed and/or of a more uniform grain size distribution (Hapke, 1986, 1993) than the surface materials of Arabia Terra and Mare Acidalium.

The single-scattering albedo fit to the Hapke function ranged from $0.6 < w < 0.7$ for lower-albedo regions and $0.8 < w < 0.9$ for higher-albedo regions at 673, 953, and 1042 nm, and was relatively constant for all surfaces at 502 nm with $w \sim 0.35$. The decrease in w at 502 nm is consistent with the presence of a strong Fe–O absorption shortward of ~ 600 nm (Soderblom, 1992; Bell, 1996). These values of single-scattering albedo are consistent with values previously reported (Thorpe, 1982; Arvidson et al., 1989; Guinness et al., 1997; Johnson et al., 1999; Johnson et al., 2006).

There are a large number of observations from the Mars Global Surveyor Mars Orbital Camera (Malin et al., 1998; Malin and Edgett, 2001), the Mars Express High Resolution Stereo Camera (Pinet et al., 2005), and from the Mars Exploration Rover Pancam and Navcam instruments (Seelos, 2005; Johnson et al., 2006; Soderblom et al., 2006) that cover a wide range of forward and backscattering phase angles. Such data along with other HST and/or spacecraft observations could provide better constraints on the global photometric properties of the martian surface, allowing more accurate interpretations of the physical properties of the martian surface. Additionally, such global scattering properties are critical for many application including the comparison of observations acquired under varying geometries and lighting conditions, complex atmospheric radiative transfer models, and photoclinometry studies.

Acknowledgments

References

Arvidson, R.E., Guinness, E.A., Dale-Bannister, M.A., Adams, J., Smith, M., Christensen, P.R., Singer, R.B., 1989. Nature and distribution of surficial deposits in Chryse Planitia and vicinity, Mars. J. Geophys. Res. 94, 1573–1587.

Arvidson, R.E., Bibring, J., Poulet, F., Squyres, S.W., Wolff, M., Morris, R., 2004. Coordinated Mars Exploration Rover and Mars Express OMEGA observations over Meridiani Planum. Eos (Fall Suppl.). P24A-06.

Baggett, S., Sparks, W., Ritchie, C., MacKenty, J., 1996. Contamination correction in SYNPHOT for WFPC-2 and WF/PC-1. WFPC2 Instrum. Sci. Rep. 96-02, Space Telescope Science Institute, Baltimore, MD.

Bell III, J.F., 1996. Iron, sulfate, carbonate, and hydrated minerals on Mars. In: Dyar, M.D., McCammon, C., Schaefer, M.W. (Eds.), Mineral Spectroscopy: A Tribute to Roger G. Burns. Geochemical Society Special Publication 5, Houston, pp. 359–580.

Bell III, J.F., Wolff, M., James, P., Clancy, T., Lee, S., Martin, L., 1997. Mars surface mineralogy from Hubble Space Telescope imaging during 1994–1995: Observations, calibration, and initial results. J. Geophys. Res. 102, 9109–9123.

Bell III, J.F., Wolff, M.J., Daley, T.C., Crisp, D., James, P.B., Lee, S.W., Trauger, J.T., Evans, R.W., 1999. Near-infrared imaging of Mars from HST: Surface reflectance, photometric properties, and implications for MOLA data. Icarus 138, 25–35.

Binder, A.B., Jones, A.C., 1972. Spectrophotometric studies of the photometric function, composition, and distribution of the surface materials of Mars. J. Geophys. Res. 77, 3005–3020.

Buratti, B.J., 1983. Photometric properties of Europa and the icy satellites of Saturn. Thesis. Cornell University, Ithaca, NY.

Buratti, B.J., 1984. Voyager disk resolved photometry of the saturnian satellites. Icarus 59, 392–405.

Buratti, B.J., 1995. Photometry of surface structure of the icy Galilean satellites. J. Geophys. Res. 100, 19061–19066.

Buratti, B.J., Veverka, J., 1983. Voyager photometry of Europa. Icarus 55, 93–110.

Buratti, B.J., Hicks, M.D., Soderblom, L.A., Britt, D., Oberst, J., Hillier, J.K., 2004. Deep Space 1 photometry of the nucleus of Comet 19P/Borrelly. Icarus 167, 16–29.

Burrows, C.J. (Ed.), 1995. Wide Field and Planetary Camera 2 Instrument Handbook, Version 3.0. Space Telescope Science Institute, Baltimore, MD.

Chandrasekhar, S., 1960. Radiative Transfer. Dover, New York.

Christensen, P.R., Bandfield, J.L., Hamilton, V.E., Ruff, S.W., Kieffer, H.H., Titus, T.N., Malin, M.C., Morris, R.V., Lane, M.D., Clark, R.L., Jakosky, B.M., Mellon, M.T., Pearl, J.C., Conrath, B.J., Smith, M.D., Clancy, R.T., Kuzmin, R.O., Roush, T., Mehall, G.L., Gorelick, N., Bender, K., Murray, K., Dason, S., Greene, E., Silverman, S., Greenfield, M., 2001. Mars Global Surveyor Thermal Emission Spectrometer experiment: Investigation description and surface science results. J. Geophys. Res. 106, 23823–23872.

Clancy, R.T., Wolff, M.J., Christensen, P.R., 2003. Mars aerosol studies with the MGS TES emission phase function observations: Optical depths, particle sizes, and ice cloud types versus latitude and solar longitude. J. Geophys. Res. 108 (E9), doi:10.1029/2003JE002058. 5098.

Cord, A., Pinet, P.C., Chevrel, S.D., Daydou, Y., Shkuratov, Y.G., Stankevich, D.G., Petrov, D.V., 2004. Physical meaning of the Hapke parameter for macroscopic roughness: Experimental determination for planetary regolith surface analogs and numerical approach. Proc. Lunar Sci. Conf. 35. Abstract 1708.

Domingue, D., Hapke, B., 1992. Disk resolved photometric analysis of Europan terrains. Icarus 99, 70–81.

Domingue, D.L., Hapke, B.W., Lockwood, G.W., Thompson, D.T., 1991. Europa's phase curve: Implications for surface structures. Icarus 90, 30–42.

Domingue, D., Hartman, B., Verbiscer, A., 1997. The scattering properties of natural terrestrial snows versus icy satellite surfaces. Icarus 128, 28–48.

Erard, S., 2000. The 1994–1995 apparition of Mars observed from Pic-du-Midi. Planet. Space Sci. 48, 1271–1287.

Erard, S., Mustard, J., Murchie, S., Bibring, J.P., Cerroni, P., Coradini, A., 1994. Martian aerosols: Near-infrared spectral properties and effects on the observation of the surface. Icarus 111, 317–337.

Esposito, F., Giuranna, M., Maturilli, A., Palomba, E., Colangeli, L., Formisano, V., 2006. Albedo and photometric study of Mars with the planetary spectrometer onboard the Mars express mission. Icarus. Submitted for publication.

Geissler, P.E., 2005. Three decades of martian surface changes. J. Geophys. Res. 110 (E02001), doi:10.1029/2004JE002345.

Geissler, P.E., Greenberg, R., Hoppa, G., McEwen, A., Tufts, R., Phillips, C., Clark, B., Ockert-Bell, M., Helfenstein, P., Burns, J., Veverka, J., Sullivan, R., Greeley, R., Pappalardo, R.T., Head, J.W., Belton, M.J.S., Denk, T., 1998. Evolution of lineaments on Europa: Clues from Galileo multispectral imaging observations. Icarus 135, 107–126.

Geissler, P.E., McEwen, A., Keszthelyi, L., Lopes-Gautier, R., Granahan, J., Simonelli, D.P., 1999. Global color variations on IO. Icarus 140, 265–282.

Goguen, J.D., 1981. A theoretical and experimental investigation of the photometric functions of particulate surfaces. Thesis. Cornell University, Ithaca, NY.

Gradie, J., Veverka, J., 1984. Photometric properties of powered sulfur. Icarus 58, 227–245.

Greeley, R., Thompson, S.D., Whelley, P.L., Squyres, S., Neukum, G., Arvidson, R., Malin, M., Kuzmin, R., Christensen, P., Rafkin, S., Michaels, T., Pinet, P., Joliff, B., Cabrol, N., Richter, L., Hauber, E., Hoffmann, H., Jaumann, R., the Athena Science Team, the HRSC Science Team, the THEMIS Science Team, and the MOC Science Team, 2004. Coordinated observations of aeolian features from the Mars Exploration Rovers (MER) and the Mars Express High Resolution Stereo Camera and other orbiters. Proc. Lunar Sci. Conf. 35. Abstract 2162.

de Grenier, M., Pinet, P.C., 1995. Near-opposition martian limb-darkening: Quantification and implication for visible–near-infrared bidirectional reflectance studies. Icarus 115, 354–368.

Guinness, E.W., 1981. Spectral properties (0.04 to 0.75 microns) of soils exposed at the Viking 1 Lander site. J. Geophys. Res. 86, 7983–7992.

Guinness, E.W., Arvidson, R.E., Clark, I., Shepard, M.K., 1997. Optical scattering properties of terrestrial varnished basalts compared with rocks and soils at the Viking Lander sites. J. Geophys. Res. 102, 28687–28703.

Hapke, B., 1981. Bidirectional reflectance spectroscopy. 1. Theory. J. Geophys. Res. 86, 3039–3054.

Hapke, B., 1984. Bidirectional reflectance spectroscopy. 3. Correction for macroscopic roughness. Icarus 59, 41–59.

Hapke, B., 1986. Bidirectional reflectance spectroscopy. 4. The extinction coefficient and the opposition effect. Icarus 67, 264–280.

Hapke, B., 1993. Theory of Reflectance and Emittance Spectroscopy. Cambridge Univ. Press, New York.

Hapke, B., 2002. Bidirectional reflectance spectroscopy. 5. The coherent backscatter opposition effect and anisotropic scattering. Icarus 157, 523–534.

Hapke, B., Nelson, R., Smythe, W., 1993. The opposition effect of the Moon: The contribution of coherent backscattering. Science 260, 509–511.

Hapke, B., Nelson, R., Smythe, W., 1998. The opposition effect of the Moon: Coherent backscattering and shadow hiding. Icarus 133, 89–97.

Hartman, B.N., Domingue, D., Verbiscer, A., 1996. Scattering of light by individual particles and the implications for models of planetary surfaces. Proc. Lunar Sci. Conf. 27. Abstract 495.

Helfenstein, P., Shepard, M.K., 1999. Submillimeter-scale topography of the lunar regolith. Icarus 141, 107–131.

Helfenstein, P., Shepard, M.K., 2003. A Blind test of Hapke's photometric model. Proc. Lunar Sci. Conf. 34. Abstract 1968.

Helfenstein, P., Veverka, J., 1987. Photometric properties of lunar terrains derived from Hapke's equation. Icarus 72, 342–357.

Helfenstein, P., Veverka, J., 1989. Physical characteristics of asteroid surfaces from photometric analysis. In: Binzel, R., Gehrels, T., Matthews, M.S. (Eds.), Asteroids II. Univ. of Arizona Press, Tucson, pp. 557–593.

Helfenstein, P., Veverka, J., Thomas, P.C., Simonelli, D.P., Klaasen, K., Johnson, T.V., Fanale, F., Granahan, J., McEwen, A.S., Belton, M., Chapman, C., 1996. Galileo photometry of Asteroid 243 Ida. Icarus 120, 48–65.

Helfenstein, P., Veverka, J., Hillier, J., 1997. The lunar opposition effect: A test of alternative models. Icarus 128, 2–14.

Henyey, L.G., Greenstein, J., 1941. Diffuse radiation in the galaxy. Astrophys. J. 93, 70–83.

Herkenhoff, K.E., Murray, B.C., 1990. High-resolution topography and albedo of the South Polar layered deposits on Mars. J. Geophys. Res. 95, 14511–14529.

Hillier, J.K., Veverka, J., Helfenstein, P., Lee, P., 1994. Photometric diversity of terrains on Triton. Icarus 109, 296–312.

Holtzman, J.A., Hester, J.J., Casertano, S., Trauger, J.T., Watson, A.M., Ballester, G.E., Burrows, C.J., Clarke, J.T., Crisp, D., Evans, E., 1995a. The performance and calibration of WFPC2 on the Hubble Space Telescope. Publ. Astron. Soc. Pacific 107, 156–178.

Holtzman, J.A., Burrows, C.J., Casertano, S., Hester, J.J., Trauger, J.T., Watson, A.M., Worthey, G., 1995b. The photometric performance and calibration of WFPC2. Publ. Astron. Soc. Pacific 107, 1065–1093.

Johnson, J.R., Kirk, R., Soderblom, L.A., Gaddis, L., Reid, R.J., Britt, D.T., Smith, P., Lemmon, M., Thomas, N., Bell III, J.F., Bridges, N.T., Anderson, R., Herkenhoff, K.E., Maki, J., Murchie, S., Dummel, A., Jaumann,

R., Hauber, E., Arnold, G., 1999. Photometric properties of materials at the Sagan Memorial Station, Mars. J. Geophys. Res. 104, 8809–8830.

Johnson, J.R., Grundy, W.M., Lemmon, M.T., Bell III, J.F., Johnson, M.J., Deen, R., Arvidson, R.E., Farrand, W.H., Guinness, E., Hayes, A.G., Herkenhoff, K.E., Seelos IV, F., Soderblom, J., Squyres, S., 2006. Spectrophotometric properties of materials observed by Pancam on the Mars Exploration Rovers. 1. Spirit. J. Geophys. Res. 111 (E02S14), doi:10.1029/2005JE002494.

Kirk, R.L., Howington-Kraus, E., Redding, B., Galuszka, D., Hare, T.M., Archinal, B.A., Soderblom, L.A., Barrett, J.M., 2003. High-resolution topomapping of candidate MER landing sites with Mars Orbiter Camera Narrow-angle images. J. Geophys. Res. 108 (E12), doi:10.1029/2003JE002131.

Lambert, J.H., 1760. Photometria Sive de Mensura et Gradibus Luminis, Colorum et Umbrae. Detleffsen, Augsburg.

Lauer, T.R., 1989. The reduction of Wide Field/Planetary Camera images. Publ. Astron. Soc. Pacific 101, 445–469.

Levenberg, K.A., 1944. Method for the solution of certain non-linear problems in least-squares. Quart. Appl. Math. 2, 164–168.

Malin, M.C., Edgett, K.S., 2001. Mars Global Surveyor Mars Orbiter Camera: Interplanetary cruise through primary mission. J. Geophys. Res. 106, 23429–23570.

Malin, M.C., Carr, M.H., Danielson, G.E., Davies, M.E., Hartmann, W.K., Ingersoll, A.P., James, P.B., Masursky, H., McEwen, A.S., Soderblom, L.A., Thomas, P., Veverka, J., Caplinger, M.A., Ravine, M.A., Soulanille, T.A., Warren, J.L., 1998. Early views of the martian surface from the Mars Orbiter Camera of Mars Global Surveyor. Science 279, 1681–1685.

Marquardt, D.W., 1963. An algorithm for least-squares estimation of non-linear parameters. J. Soc. Ind. Appl. Math. 11, 431–441.

McEwen, A.S., 1986. Exogenic and endogenic albedo and color patterns on Europa. J. Geophys. Res. 91, 8077–8097.

McEwen, A.S., 1991. Photometric functions for photoclinometry and other applications. Icarus 92, 298–311.

McGuire, A.F., Hapke, B.W., 1995. An experimental study of light scattering by large, irregular particles. Icarus 113, 134–155.

Mead, J.M., 1970. The contribution of atmospheric aerosols to the martian opposition effect. Icarus 13, 82–95.

Meador, W.E., Weaver, W.R., 1975. A photometric function for diffuse reflection by particulate materials. NASA Tech. Note D-7903.

Mellon, M.T., Jakosky, B.M., Kieffer, H.H., Christensen, P.R., 2000. High-resolution thermal-inertia mapping from the Mars Global Surveyor Thermal Emission Spectrometer. Icarus 148, 437–455.

Minnaert, M., 1941. The reciprocity principle in lunar photometry. Astrophys. J. 93, 403–410.

O'Leary, B.T., Rea, D.G., 1968. The opposition effect of Mars and its implications. Icarus 9, 405–428.

Paige, D.A., Keegan, K.D., 1994. Thermal and albedo mapping of the polar regions of Mars using Viking thermal mapper observations. 2. South polar region. J. Geophys. Res. 99, 25993–26014.

Paige, D.A., Bachman, J.E., Keegan, K.D., 1994. Thermal and albedo mapping of the polar regions of Mars using Viking thermal mapper observations. 1. North polar region. J. Geophys. Res. 99, 25959–25991.

Pappalardo, R.T., Head, J.W., Collins, G.C., Kirk, R.L., Neukum, G., Oberst, J., Giese, B., Greeley, R., Chapman, C.R., Helfenstein, P., Moore, J.M., McEwen, A., Tufts, B.R., Senske, D.A., Breneman, H.H., Klaasen, K., 1998. Grooved terrain on Ganymede: First results from Galileo high-resolution imaging. Icarus 135, 276–302.

Pinet, P.C., Cord, A., Jehl, A., Daydou, Y., Chevrel, S., Baratoux, D., Greeley, R., Neukum, G., Bell III, J.F., MEX/HRSC Co-I Team, and the MER/Athena Science Team, 2005. Orbital imaging photometry and surface geologic processes within Gusev. In: EGU Spring 2005 Conf. Abstract EGU05-A-09363.

Pleskot, L.K., Miner, E.D., 1981. Time variability of martian bolometric albedo. Icarus 45, 179–201.

Pollack, J.B., Colburn, D., Flasar, F.M., Kahn, R., Carlston, C., Pidek, D., 1979. Properties and effects of dust particles suspended in the martian atmosphere. J. Geophys. Res. 84, 2929–2945.

Poulet, F., Arvidson, R., Bibring, J.-P., Squyres, S., Langevin, Y., Gondet, B., Gendrin, A., the OMEGA Science Team, and the Athena Science Team,

2004. Mars Express OMEGA observations of the Mars Exploration Rover sites and coordinated analyses. Bull. Am. Astron. Soc. 36. Abstract 31.06.

Seelos, F.P., 2005. Multispectral photometric properties of the martian surface at the Mars Exploration Rover Landing Sites. Thesis. Washington University in St. Louis, St. Louis, MO.

Shkuratov, Y.G., Muinonen, K., 1992. Interpreting asteroid photometry and polarimetry using a model of shadowing and coherent backscattering. Acm. Proc., 549–552.

Smith, M.D., Pearl, J.C., Conrath, B.J., Christensen, P.R., 2000. Mars Global Surveyor Thermal Emission Spectrometer (TES) observations of dust opacity during aerobraking and science phasing. J. Geophys. Res. 105, 9539–9552.

Smith, M.D., Pearl, J.C., Conrath, B.J., Christensen, P.R., 2001. Thermal Emission Spectrometer results: Mars atmospheric thermal structure and aerosol distribution. J. Geophys. Res. 106, 23929–23945.

Soderblom, L.A., 1992. The composition and mineralogy of the martian surface from spectroscopic observations: 0.3–50 µm. In: Kieffer, H.H., Jakosky, B.M., Snyder, C.W., Matthews, M.S. (Eds.), Mars. Univ. of Arizona Press, Tucson, pp. 557–593.

Soderblom, L.A., Kirk, R.L., 2003. Meter-Scale 3-D models of the martian surface from combining MOC and MOLA data. Proc. Lunar Sci. Conf. 34. Abstract 1730.

Soderblom, J.M., Bell III, J.F., Johnson, J.R., Maki, J.N., Wolff, M.J., 2006. Photometry of the martian surface using data from the Navigation Cameras on the Mars Exploration Rovers Spirit and Opportunity. Proc. Lunar Sci. Conf. 37. Abstract 1935.

Squyres, S.W., 1981. The morphology and evolution of Ganymede and Callisto. Thesis. Cornell University, Ithaca, NY.

Squyres, S.W., Veverka, J., 1981. Voyager photometry of surface features on Ganymede and Callisto. Icarus 46, 137–155.

Sullivan, R., Greeley, R., Pappalardo, R., Asphaug, E., Moore, J.M., Morrison, D., Belton, M.J.S., Carr, M., Chapman, C.R., Geissler, P., Greenberg, R., Granahan, J., Head III, J.W., Kirk, R., McEwen, A., Lee, P., Thomas, P.C., Veverka, J., 1996. Geology of 243 Ida. Icarus 120, 119–139.

Thomas, N., 2001. Light scattering in the martian atmosphere: Effects on surface photometry. In: Williams, I.P., Thomas, N. (Eds.), Solar and Extra-Solar Planetary Systems. In: Lecture Notes in Physics, vol. 577. Springer-Verlag, New York, pp. 191–204.

Thorpe, T.E., 1982. Martian surface properties indicated by the opposition effect. Icarus 49, 398–415.

Tomasko, M.G., Doose, L.R., Lemmon, M., Smith, P.H., Wegryn, E., 1999. Properties of dust in the martian atmosphere from the Imager on Mars Pathfinder. J. Geophys. Res. 104, 8987–9007.

de Vaucouleurs, D., 1968. On the opposition effect of Mars. Icarus 9, 598–599.

Veverka, J., Goguen, J., Yang, S., Elliot, J.L., 1978. Near-opposition limb darkening of planetary interest. Icarus 33, 368–379.

Vdovichenko, V.D., Nosova, T.P., Kirienko, G.A., 1997. Spectrophotometry of Mars during the 1992–1993 visibility period. Solar Syst. Res. 32, 198–206.

Wolff, M.J., Clancy, T.R., 2003. Constrains on the size of martian aerosols form Thermal Emission Spectrometer observation. J. Geophys. Res. 108 (E9), doi:10.1029/2003JE002057. 5097.

Wolff, M.J., Lee, S.W., Clancy, R.T., Martin, L.J., James, P.B., Bell III, J.F., 1997. Observations of dust storms on Mars with the Hubble Space Telescope. J. Geophys. Res. 102, 1679–1692.

Wolff, M.J., Bell III, J.F., James, P.B., Clancy, R.T., Lee, S.W., 1999. Hubble Space Telescope observations of the martian aphelion cloud belt prior to the Mars Pathfinder mission: Water-ice cloud and dust optical depths. J. Geophys. Res. 104, 9027–9042.

Young, A.T., 1975. UBV photometry of Mars. In: Woszczyk, A., Iwaniszewska, C. (Eds.), Exploration of the Planetary System. Reidel, Boston, MA, pp. 253–285.